

Cross-linked matrix rigidity and soluble retinoids synergize in nuclear lamina regulation of stem cell differentiation

Irena L. Ivanovska, Joe Swift, Kyle Spinler, Dave Dingal, Sangkyun Cho, and Dennis E. Discher*

Molecular and Cell Biophysics Lab, University of Pennsylvania, Philadelphia, PA 19104

ABSTRACT Synergistic cues from extracellular matrix and soluble factors are often obscure in differentiation. Here the rigidity of cross-linked collagen synergizes with retinoids in the osteogenesis of human marrow mesenchymal stem cells (MSCs). Collagen nanofilms serve as a model matrix that MSCs can easily deform unless the film is enzymatically cross-linked, which promotes the spreading of cells and the stiffening of nuclei as both actomyosin assembly and nucleoskeletal lamin-A increase. Expression of lamin-A is known to be controlled by retinoic acid receptor (RAR) transcription factors, but soft matrix prevents any response to any retinoids. Rigid matrix is needed to induce rapid nuclear accumulation of the RARG isoform and for RARG-specific antagonist to increase or maintain expression of lamin-A as well as for RARG-agonist to repress expression. A progerin allele of lamin-A is regulated in the same manner in iPSC-derived MSCs. Rigid matrices are further required for eventual expression of osteogenic markers, and RARG-antagonist strongly drives lamin-A-dependent osteogenesis on rigid substrates, with pretreated xenografts calcifying *in vivo* to a similar extent as native bone. Proteomics-detected targets of mechanosensitive lamin-A and retinoids underscore the convergent synergy of insoluble and soluble cues in differentiation.

Monitoring Editor

Alex Dunn
Stanford University

Received: Jan 9, 2017

Revised: May 9, 2017

Accepted: May 26, 2017

INTRODUCTION

Stem cells differentiate in response to microenvironmental cues that derive from surrounding matrix, cell contacts, and soluble factors (Fuchs *et al.*, 2004; Engler *et al.*, 2006; Nelson and Bissell, 2006), but synergy and convergence between cues is understudied (Figure 1A). Mesenchymal stem cells (MSCs) are classically isolated by adhesion to rigid plastic (Pittenger *et al.*, 1999) but are clearly affected in differentiation by the stiffness of a synthetic gel with matrix ligand (Engler *et al.*, 2006), as well as by many soluble factors, such as retinoic acid (RA; Swift *et al.*, 2013b) which widely regulates RA receptor (RAR) transcription factors in differentiation (Williams *et al.*,

2009). MSCs in bone marrow contribute to osteogenesis (Park *et al.*, 2012), but they also reside in many tissues within perivascular niches, where they contribute to fibrosis, and some differentiated lineages (Kramann *et al.*, 2015), as well as neoplasms (Medyouf *et al.*, 2014). Many recent studies of differentiation and disease with various stem cells and gels (e.g., Musah *et al.*, 2014) have left unaddressed whether one key *physiological* modification that should stiffen matrix, namely enzymatic cross-linking, can affect the differentiation effects of equally *physiological* soluble factors such as RA. Stiffening of bulk matrix by enzymatic cross-linking affects cancer cells *in vitro* and *in vivo* (Cox *et al.*, 2013), but differentiation studies at the single-cell scale with nanocontrol of cross-linking could provide deeper insight into synergy of matrix elasticity with a potent soluble factor such as RA.

Collagen-I is not only the most abundant protein in animals and a well-known target of enzymatic cross-linking, but it is also intrinsically proosteogenic (Yener *et al.*, 2008). Cells attach to collagenous matrix and use actomyosin forces to pull on it (Discher *et al.*, 2005), with stiff matrices driving cytoskeleton assembly and cell spreading within hours (Engler *et al.*, 2006). Nuclei flatten and also spread with the cell, and the level of the “keratin-like” nuclear protein lamin-A increases, consistent with lamin-A (but not lamin-B) being high in collagen-rich tissues such as bone but low in soft tissues with low

This article was published online ahead of print in MBoC in Press (<http://www.molbiolcell.org/cgi/doi/10.1091/mbc.E17-01-0010>) on May 31, 2017.

*Address correspondence to: Dennis E. Discher (discher@seas.upenn.edu).

Abbreviations used: AFM, atomic force microscope; ALP, alkaline phosphatase; E, Young's modulus of elasticity or stiffness; GFP, green fluorescent protein; iPSC, induced pluripotent stem cells; MS, mass spectrometry; MSC, mesenchymal stem cell; OIM, osteoinduction media; RA, retinoic acid; RAR, retinoic acid receptor.

© 2017 Ivanovska *et al.* This article is distributed by The American Society for Cell Biology under license from the author(s). Two months after publication it is available to the public under an Attribution–Noncommercial–Share Alike 3.0 Unported Creative Commons License (<http://creativecommons.org/licenses/by-nc-sa/3.0>).

“ASCB®,” “The American Society for Cell Biology®,” and “Molecular Biology of the Cell®” are registered trademarks of The American Society for Cell Biology.

Supplemental Material can be found at:
<http://www.molbiolcell.org/content/suppl/2017/05/29/mbc.E17-01-0010v1.DC1>

collagen such as marrow and brain (Swift *et al.*, 2013b). Lamin-A mutations affect many stiff tissues, as illustrated by defects in muscle, bone, and skin in the accelerated aging syndrome progeria, whereas soft tissues remain unaffected (Bridger *et al.*, 2007). Such observations suggest matrix-linked regulatory roles for lamins, and recent surprising results for lamin levels in MSCs on gels further show that retinoid regulation occurs only with cells on stiff substrates as opposed to soft gels (Swift *et al.*, 2013b). Promoter-reporter approaches have already shown that the promoter region of the *LMNA* gene binds RAR transcription factors (Okumura *et al.*, 2004), so that changes in lamin-A message can be caused by at least some retinoids in culture. However, it is unclear which of the three known RAR isoforms (RARA, RARB, and/or RARG) and which (if any) isoform-specific soluble factors are relevant to regulation in MSCs, especially when cultured on physiological matrices with enzymatic cross-linking.

Here stiffness measurements of the tibia's osteogenic niche are followed by meta-analyses of transcriptomes from tissues that span a wide range of stiffness and that suggest general associations of collagen-I with matrix cross-linking, myosin contractile forces, lamin-A, RARG, and osteogenic induction. These tissue-level associations are all observed in culture with naive MSCs on collagen-I nanofilms that are cross-linked rather than pristine, and the results map into gels of suitable effective stiffness. RARG's nuclear localization primarily in cells on stiff substrates helps to explain the rigidity-dependent regulation of lamin-A expression by soluble RARG agonists/antagonists, and the findings are extended to lamin-A's "progerin" splice-form in induced pluripotent stem cell (iPSC)-derived MSCs from a progeria patient (Olive *et al.*, 2010). Matrix rigidity synergizes with RARG agonist suppression of normal and progerin lamin-A, and rigidity also synergizes with RARG antagonist to increase lamin-A and enhance osteogenesis in vitro and in vivo. The approach is

likely relevant to fibrosis of the perivascular niche (Kramann *et al.*, 2015), in which a thin layer of matrix is enriched in cross-linked collagen-1 to drive—in the absence of osteogenic soluble factors—a fibrogenic phenotype with high actomyosin contractility, lamin-A, and RARG (Dingal *et al.*, 2015).

RESULTS

Cell-scale stiffness of the osteogenic niche

In bone formation, MSCs egress from a niche that is likely perivascular and migrate to a precalcified surface in differentiation to osteoblasts (Park *et al.*, 2012). In vitro studies show that matrix stiffness directs MSC migration (Raab *et al.*, 2012) as well as differentiation (Engler *et al.*, 2006), and yet no measurements exist for the in situ mechanical properties of osteoid matrix at the microscale to which a cell adheres and probes. For cartilage, atomic force microscopy (AFM) has been used (Stolz *et al.*, 2009) to measure an interstitial elastic modulus E at a scale that approximates that of the matrix surrounding chondrocytes (Guilak *et al.*, 2005) but also proves to be 10-fold or more softer than the macroscopic rigidity of cartilage.

To study the osteogenic niche in bone, we sliced mouse tibia along its length (Figure 1B) and applied AFM nanoindentation (Figure 1C) to the exposed marrow and then to the inner surface of bone after washing away marrow. Samples were fixed and stained for alkaline phosphatase (ALP) activity, which confirmed the presence of osteoblastic cells (Figure 1D), and high-resolution AFM imaging revealed fibrillar matrix (Figure 1E). Force-indentation data (Figure 1F) revealed E for marrow to be ~0.1 kPa versus a much stiffer bone surface with peaks at 2, 30, and 100 kPa (Figure 1G). The softest peak is close to E for isolated cells of mesenchymal origin (Titushkin and Cho, 2007; Yourek *et al.*, 2007; Darling *et al.*, 2008; Yim *et al.*, 2010). The 30- and 100-kPa

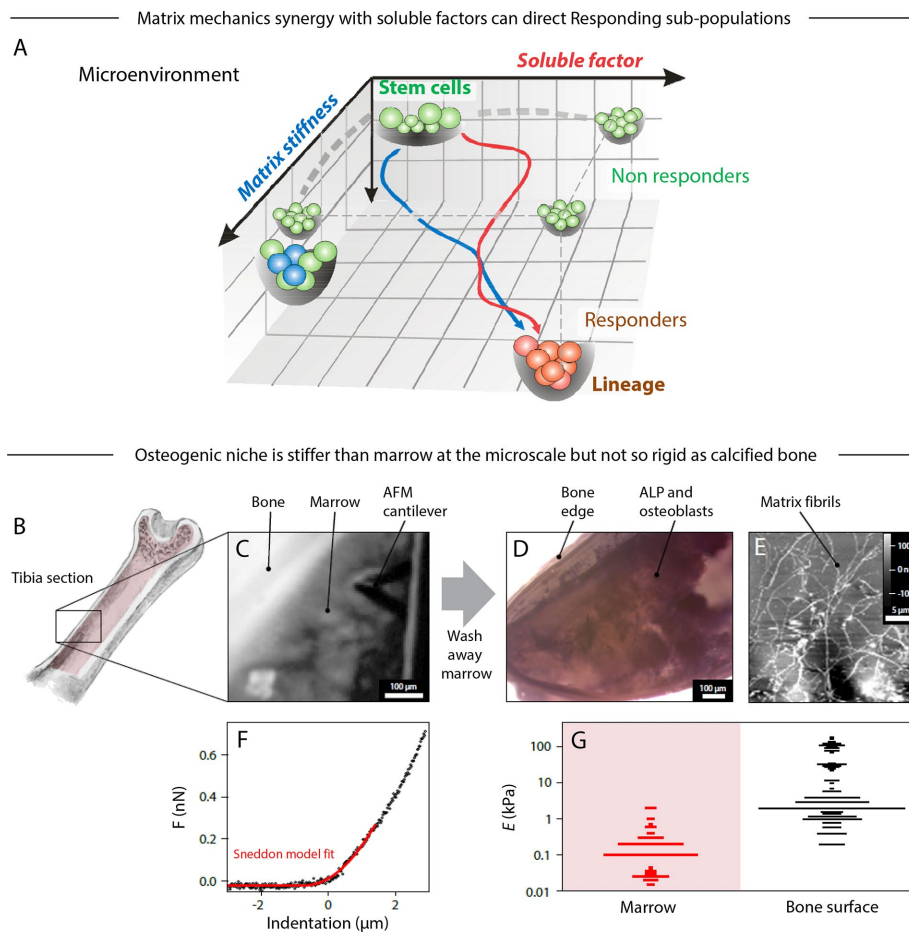


FIGURE 1: The bone microenvironment defines mechanical and molecular properties that influence the trajectory of stem cell differentiation. (A) The fate of a stem cell on a Waddington-like landscape is potentially influenced by matrix properties in synergy with soluble factors. One example is osteogenesis of bone marrow MSC. However, differentiation might also include subpopulations that are not responsive to either stimuli or their combination. (B) Mouse trabecular bone was cut and opened to expose the tissue inside for probing by AFM. (C) Bright-field image showing bone marrow probed in situ by AFM. The bone marrow was subsequently washed away and the remaining tissue and osteoid reexamined. (D) Bone tissue stained for ALP activity. (E) Contact-mode AFM image of the exposed bone, showing extracellular matrix fibers as part of the osteoid. (F) A typical force-indentation curve of bone marrow (prewash), fitted with a modified Hertz model for a conical probe (red). (G) Comparison of the distributions of Young's modulus, E , measured by AFM at different locations in the prewashed marrow, which is soft, and exposed osteoid, which is typically stiffer. All experiments, $n \geq 3$ (mean + SEM).

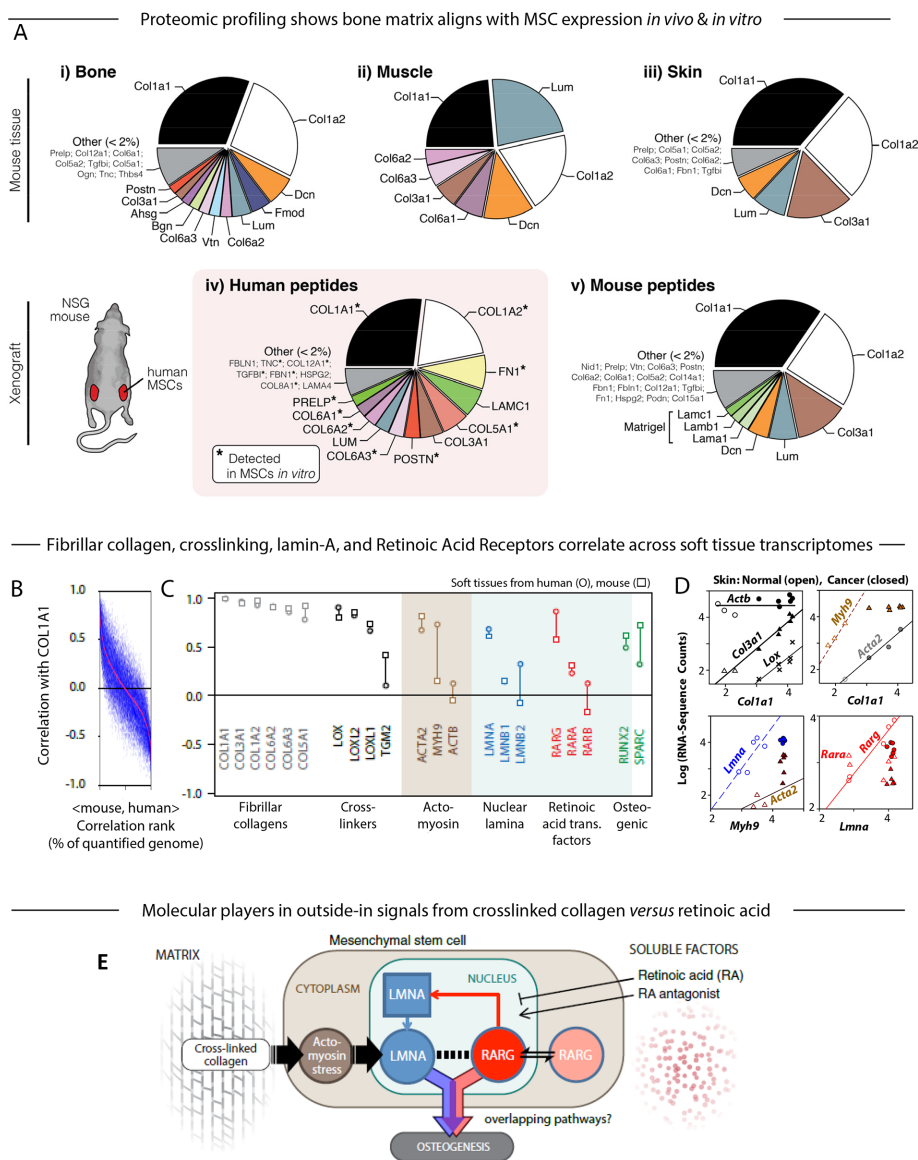


FIGURE 2: Proteomic and transcriptomic profiles of mouse tissue and human xenografts suggest the key components in a model of the microenvironment-to-osteogenesis signaling cascade. (A) Whole mouse tissues (i, bone; ii, muscle; iii, skin) were profiled by MS proteomics and the ratios of mean ion currents used to estimate the fractional compositions of the respective extracellular matrices. In all cases, the matrix was dominated by collagen-I. Human MSCs were also engrafted into mouse flank, excised after 4 wk, and examined by MS. Subsequent analysis allowed separate identification and quantification of mouse and human peptides (Supplemental Figure S1A; Swift et al., 2013a,b). The human peptides in the xenograft (iv) showed some similarity to the endogenous bone profile, and most of the detectable matrix proteins were also present in preengraftment MSCs (asterisk). Mouse peptides in the xenograft (v) suggested comparison to skin, perhaps unsurprising, given the location of the graft, and also showed likely remnants of the Matrigel component of the initial injection. (B) Pearson correlation between primary matrix component COL1A1 mRNA and other genes quantified in soft tissues of mouse and human (genes with common annotation, $n \approx 15,000$), sorted by the mean Pearson coefficient in mouse and human (red line). (C) Pearson correlation between COL1A1 and transcripts for fibrillar collagens, cross-linking enzymes, actomyosin cytoskeleton proteins, nuclear lamina proteins, RAR, and osteogenic transcription factors. Many of these key components were in the top few percent of correlations with collagen-I, as seen by comparison to Figure 2B. (D) RNA-sequencing data from mouse skin of normal or induced squamous cell carcinomas (SCCs; Friedrichs et al., 2007) revealing power-law relations between many of the factors analyzed in C. (E) Gene circuit model of how extracellular factors, mechanical (matrix composition and cross-linking) and molecular (soluble factors such as RA), can influence MSC osteogenesis. Matrix stiffness induces stress in the actomyosin network, which feeds into levels of nucleoskeletal protein LMNA (Buxboim et al., 2014); LMNA regulates its own transcript RARG, which in turn can be modulated by soluble

peaks could reflect the elastic response and the spatial heterogeneity of the mineralized matrix due to the presence of interfibrillar and extrafibrillar bioapatite (Alexander et al., 2012). Stiffer substances were also detected and likely correspond to calcified bone (on the order of gigapascals) but cannot be resolved with soft cantilevers. The 30-kPa peak is consistent with E of the osteoid matrix secreted by cultured osteoblasts (Engler et al., 2006). Osteogenesis is thus associated with stiffer tissue than the marrow space that is filled with hematopoietic cells. To address whether such stiff matrix has osteogenic specificity or not, we made a compositional comparison to other collagen-rich tissues.

Proteomic and transcriptomic meta-analysis identify possible factors in MSC osteogenesis

Mass spectrometry (MS) proteomics of bone compared with two other stiff tissues, muscle and skin (Figure 2A, i–iii), showed that all had an abundance of collagen-I (Col1a1 and Col1a2). Collagen-1 is not only the most abundant protein in our bodies (Neuman and Logan, 1950) and a key determinant of tissue mechanics (Swift et al., 2013b), but it is also the main scaffold protein of osteoid that acts together with soluble factors in a niche for MSC osteogenesis and bone mineralization (Katz and Li, 1973; Stein et al., 1990). To provide evidence for such a process, we cultured human MSCs with standard osteogenic soluble factors, engrafted them into mouse flanks, and excised them after 4 wk for profiling by MS. Human-specific peptides were $\sim 10\%$ of all peptides (Supplemental Figure S1A), and overall profiles (Swift et al., 2013a,b) compare well to MSC cultures (Figure 2A, iv and v), with a matrix complexity similar to mouse bone rather than mouse skin at the graft site. Of interest, periostin is known to activate the cross-linking enzyme lysyl oxidase (Lox), which stiffens collagen (Maruhashi et al., 2010).

MS profiling of tissues shows that stiffer tissues have more fibrillar collagen (with bone > muscle > fat > brain), and so for a

agonists and antagonists to the RA pathway (Swift et al., 2013b). Both LMNA, through regulation of the SRF pathway (Ho et al., 2013; Swift et al., 2013b; Buxboim et al., 2014; Talwar et al., 2014), and the RA pathway conceivably contribute to an osteogenic endpoint, but the extent of overlap between these pathways is not known (Figure 1A). All experiments, $n \geq 3$ (mean + SEM).

diverse set of tissues, we conducted a meta-analysis of transcriptomes to ask what transcripts generically associate with collagen-I (*COL1A1*) in human and mouse (Figure 2B). A wide range of soft through stiff tissues was analyzed because MSCs are found in most tissues beyond marrow (Kramann *et al.*, 2015), and MSCs can be induced toward many tissue lineages. Bone transcriptomes were excluded so that the generic nature of any correlations might be assessed in an unbiased way with MSC cultures and osteoinduction. *COL1A1* mRNA scaled with protein across many tissues (Supplemental Figure S1B), and the top few percent of *COL1A1*-correlated transcripts suggests generic relationships with 1) collagen cross-linking,

2) a tensed actomyosin cytoskeleton, 3) a stiff nucleus with high lamin-A, and 4) osteogenesis (Figure 2C). Fibrillar collagens generally correlate with *COL1A1*, as do enzymes that cross-link collagen, particularly *LOX*, but also tissue transglutaminase (*TGM2*) to a more limited extent. Smooth muscle actin (*ACTA2*) is a well-known marker of cytoskeleton tension (Wipff *et al.*, 2007), as is nonmuscle myosin-IIA (*MYH9*), and both correlate with *COL1A1*, as does nucleoskeletal lamin-A (*LMNA*), which we showed confers nuclear stiffness (Swift *et al.*, 2013b). No correlations are seen with ubiquitous β -actin (*ACTB*) or B-type lamins (*LMNB1*, *LMNB2*), with the latter consistent with near-constant protein expression across tissues (Swift *et al.*, 2013b). Lamin-A transcription is regulated by RAR transcription factors (Swift *et al.*, 2013b), but *COL1A1* correlates only with *RARG*, which is the one isoform known to contribute to osteogenesis (Williams *et al.*, 2009). Surprisingly, even though bone is not included in this meta-analysis, *COL1A1* shows moderate correlations with the early osteogenic transcription factor *RUNX2* and with the late osteogenic marker of bone matrix, *SPARC* ($p \approx 0.5$).

Skin transcriptomes from mice were analyzed in order to challenge the foregoing molecular associations and also assess their possible relevance to subcutaneous xenografts (Figure 2A). RNA-sequencing data recently produced from both healthy tissue and chemically induced squamous cell carcinoma (Nassar *et al.*, 2015) show a near linear relation versus *Col1a1* for *Col3a1*, *Lox*, and *Acta2*, whereas *Actb* is constant across both healthy and cancerous skin (Figure 2D). *Myh9* also increases with *Col1a1* in healthy tissue but remains constant in cancer. For normal tissue but not cancer, *Lmna* increases with *Myh9*, and *Rarg* (but not *Rara*) increases with *Lmna*. Therefore, together with our recent findings that stiff matrix promotes actomyosin contractile stress, which stabilizes lamin-A expression in MSCs, the foregoing meta-analyses suggest a hypothesis to test in vitro: if stiff, cross-linked collagen ultimately couples to RARG levels and nuclear localization, then both rigid matrix and RARG-specific soluble factors will jointly modulate lamin-A expression and osteogenesis (Figure 2E).

Enzymatic cross-linking stiffens collagen-I nanofilms to drive symmetric spreading of MSCs

As a minimal culture substrate to use for testing our working hypothesis, we assembled nanofilms of collagen-I on untreated mica substrates (Cisneros *et al.*, 2007) and either left the films pristine or enzymatically cross-linked them (Figure 3A). We used TGM2 for cross-linking because it is broadly expressed (Figure 2C) and required for fibronectin-collagen networks in early matrix genesis (Al-Jallad *et al.*, 2006). TGM2 is also found in bone and in osteoblastic cells associated with matrix mineralization

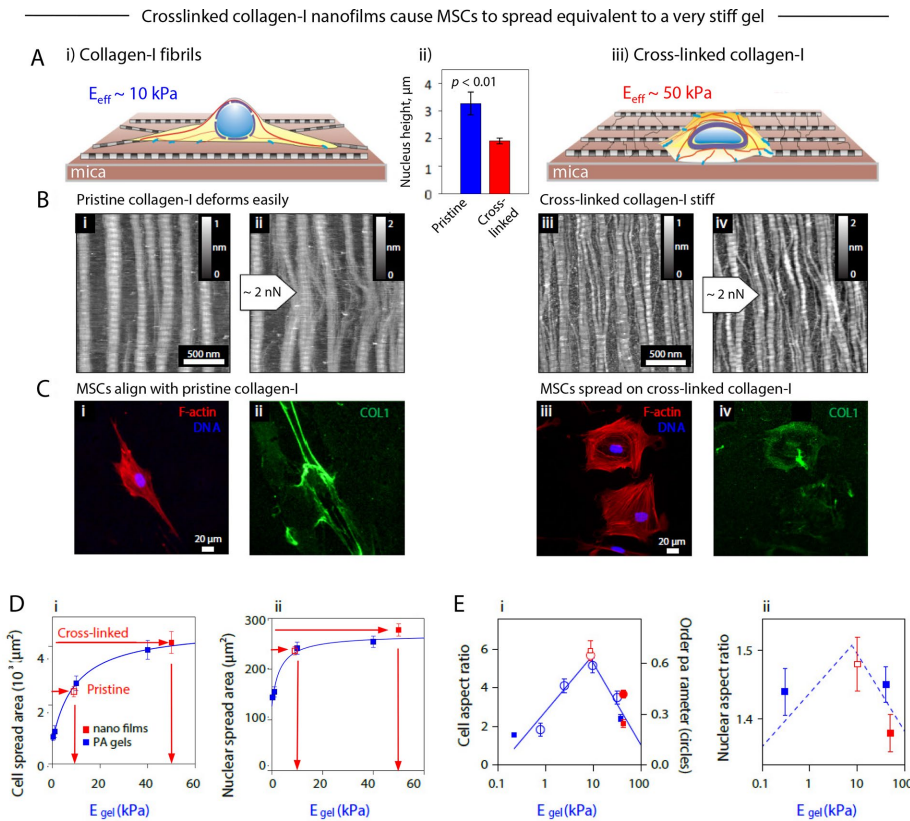


FIGURE 3: Analysis of cell morphology and protein organization in MSCs cultured on pristine and cross-linked collagen-I films shows the equivalence of cross-linking to increased matrix stiffness. (A) Thin collagen films allowed an in vitro study of the effects on MSC morphology of culture on (i) pristine and (iii) cross-linked collagen-I films; (ii) nuclear height on the two films. (B) AFM amplitude-mode topographical images of molecular films of highly ordered collagen-I fibrils, showing D-periodic structure, self-assembled on hard substrates in the absence (i, ii) and presence (iii, iv) of cross-linking. Collagen fibrils were deformed by using the AFM stylus in lithography mode to apply a low dragging force across the film (ii, iv), thus showing the flexibility of the fibrils and the deconstruction of the ribbons to monomers in the absence of cross-linking (ii). (C) Immunofluorescence images of MSCs cultured for 24 h on (i) pristine and (iii) cross-linked collagen-I films with staining against F-actin (red) and DNA (Hoechst, blue). (ii, iv) Staining against collagen showed that cross-linked films are not as severely deformed as the native ones. The random orientation of the dense regions of collagen protein suggests that the films are mechanically anisotropic, despite the topographically isotropic orientation of the fibrils evident from AFM images. (D) Comparison of matrix E-dependent cell morphologies of MSCs cultured on thick, isotropic polyacrylamide (PA) gels or thin collagen-I films. Plots of (i) cellular and (ii) nuclear spread area were fitted to hyperbolic functions, with free parameters obtained from cells on gels of controlled stiffness (blue) and cells on thin films (red squares), with the unknown effective stiffness felt by the cells on thin films superimposed to obtain the effective stiffness (10 kPa for pristine and 50 kPa for cross-linked collagen-I films). (E) Cellular aspect ratio (i, left axis), order parameter (i, right axis), and nuclear aspect ratio (ii) as functions of the gel matrix elasticity also showed consistency between morphology of pristine and cross-linked films with 10- and 40-kPa PA gels, respectively. All experiments, $n \geq 3$ (mean + SEM).

(Heath *et al.*, 2001; Kaartinen *et al.*, 2002). Collagen-I fibrils are only 300 nm long, but self-assembly of these semiflexible rods produces highly ordered fibrillar films that, regardless of cross-linking, exhibit in physiological buffers the expected D spacing of 67 nm (Meek *et al.*, 1979), as well as fibril height of 2.2 or 1.7 nm (Figure 3B, i and iii, and Supplemental Figure S2, A and B), consistent with staggered tropocollagen.

Nanofilm mechanics were altered by collagen cross-linking. Pristine films are anisotropic, with higher tensile strength in the long axes than in the perpendicular direction (Friedrichs *et al.*, 2007), and fibrils are attached to the atomically flat and rigid mica substrate only by weak electrostatic interactions, so that fibrils are readily displaced and deformed. Lateral forces on fibrils can be exerted moving an AFM tip across the surface while applying a normal force of the order of nanonewtons, which cells can easily exert via their adhesions (Discher *et al.*, 2005; Geiger *et al.*, 2009); subsequent imaging by AFM in tapping mode reveals unraveling of fibrils in pristine films, whereas cross-linked fibrils remain intact, although slightly bent (Figure 3B, ii and iv). Higher normal forces of 20 nN (Supplemental Figure S2, A and B) produced local deformations of nanofilms, which suggested that cross-linking increased film stiffness by at least twofold, consistent with earlier measurements of dialdehyde-cross-linked films (Friedrichs *et al.*, 2007). Slopes of lateral force signal versus distance were similarly higher for cross-linked than for pristine films (Supplemental Figure S2, C and D). As a further check on the effects of TGM2 addition, some MSC xenografts (Figure 2A) that were removed from mice for profiling were treated or not with TGM2 and deformed by micropipette aspiration (Majkut *et al.*, 2013). Cross-linked grafts under such stress relaxed at a slower rate than untreated grafts (Supplemental Figure S1C), which is consistent with a more solid-like response due to cross-linking.

Human bone marrow MSCs that were seeded on the nanofilms showed morphology differences within hours. On pristine nanofilms, immunofluorescence imaging showed predominantly spindle-shaped MSCs (Figure 3Ci and Supplemental Figure S2, C and D), and AFM imaging at submicrometer scales showed cell protrusions and stress fibers aligned with collagen (Supplemental Figure S2E). Immunofluorescent collagen showed that cells displace the flexible network and bundle fibrils into thick fiber bundles (Figure 3Cii) that are expected to withstand large tensions as cells adhere and pull (Friedrichs *et al.*, 2007). On cross-linked nanofilms, in contrast, MSCs exhibited a distinctly well spread and rounded osteo-like morphology (Figure 3Ciii), and collagen was not detectably displaced by cells (Figure 3Civ). Pulling forces exerted by a cell on its matrix have an (equal and) opposite action within the cell in promoting actomyosin network formation and orientation of stress fibers (Zemel *et al.*, 2010). Indeed, cells grown on pristine collagen films show tight alignment of stress fibers that is absent from cells on cross-linked nanofilms (Supplemental Figure S2, C and D).

Cell morphologies map responses on nanofilms into equivalent soft or stiff hydrogels

Synthetic polymer systems of controlled stiffness E are widely reported to drive spreading of diverse cell types (Pelham and Wang, 1997; Engler *et al.*, 2006; Geiger *et al.*, 2009), and such gels provide standards to compare to almost any other new substrate, including a nanofilm. MSCs not only spread more on stiff gels than on soft gels, but they also elongate on an intermediate E_{gel} even though gels are isotropic (Engler *et al.*, 2006; Rehfeldt *et al.*, 2012). The increased cell spread area versus E_{gel} fits a hyperbolic function independent of substrate material (Rehfeldt *et al.*, 2012), and so spread areas of the same MSCs on nanofilms here can be used to

infer an equivalent E_{gel} felt by cells (Figure 3Di). MSCs on pristine films thus spread on 10-kPa gels to the same extent, and MSCs on cross-linked films spread the same as on 50-kPa gels.

With fixed cells on stiff substrates, a large value for nuclear spread area (as a projected area) reflects nuclear flattening (Lovett *et al.*, 2013), and for live cells on the nanofilms, our AFM measurements of nuclear height confirm such flattening (Supplemental Figure S2F). Consistent with a simple flattening of the nuclear lamina in spreading on stiff substrates, total lamin-B is independent of matrix stiffness (Supplemental Figure S2Gi). In contrast, lamin-A increases in the same dual-stained MSCs (Supplemental Figure S2Gii). The increased stoichiometry for lamin-A:lamin-B versus microenvironment stiffness is consistent with *in vitro* and *in vivo* results for cancer cell lines (Swift *et al.*, 2013b) and with mRNA trends for normal tissues (Figure 2C). Nuclear projected areas are also consistent with the effective elasticities (Figure 3Dii), as are cell and nuclear aspect ratios and stress fiber alignment (Figure 3E, i and ii). Thus, whereas AFM nanoscale measurements of the films suggest a greater than twofold increase in stiffness after cross-linking, cell and nuclear morphology analyses suggest an approximately fivefold increase in the stiffness that cells sense. Of importance, because osteogenesis of MSCs on gels with $E_{\text{gel}} > 20\text{--}40$ kPa greatly exceeds that of MSCs on 10-kPa gels (Engler *et al.*, 2006; Dingal *et al.*, 2015), osteoinduction as favored by high lamin-A (Swift *et al.*, 2013b) was next hypothesized to be highest for the cross-linked nanofilms.

Cross-linked nanofilms promote myosin-II, lamin-A, RARG, and osteogenesis

Cells on soft gels are reportedly softer than cells on stiff gels (Solon *et al.*, 2007; Liu *et al.*, 2014; Pagliara *et al.*, 2014; Staunton *et al.*, 2016), but any cell indentation device such as an AFM in reality measures the effective elasticity of the cell and gel below it, analogous to two springs in series (Staunton *et al.*, 2016). The $\sim 2\text{-nm}$ films here are $\sim 1000\text{-fold}$ thinner than cells and are on rigid substrates, and so moderate indentations reveal a cell's elasticity without the need for complex decoupling of the mechanical contribution of the substrate (Figure 4A). Force-volume maps of MSCs adhering to either pristine or cross-linked nanofilms thus reveal apparent cell elasticities in the kilopascal range, with the nucleus seeming to be stiffer than perinuclear regions (Figure 4B). By probing many MSCs in the nuclear region ($\sim 1\ \mu\text{m}$ deep), this apparent nuclear stiffness of cells on cross-linked nanofilms proves approximately twofold higher than for cells on pristine collagen films (Figure 4C).

To assess the contribution of lamin-A to nuclear stiffness—which could be direct or indirect through other partners and pathways—we knocked lamin-A down by $\sim 50\%$ and found a proportional decrease in apparent nuclear stiffness (Figure 4D). This is consistent with direct contributions to stiffness of lamin-A in MSCs and other cell types as studied by micropipette aspiration, in which measurements are made after cell detachment and actin depolymerization within 1–2 h (Harada *et al.*, 2014). However, because it is also known that inhibiting the contractile actomyosin network with blebbistatin decreases “nuclear tension” through a decrease in both nuclear area and lamin-A levels in MSCs within hours, inhibition of nuclear tension should also make the nucleus measurably softer (analogous to a tensed rope being laterally stiffer until the rope is cut). An approximately fourfold reduction in the apparent nuclear stiffness with blebbistatin is indeed measured and is consistent with recent AFM studies comparing isolated nuclei to nuclei in intact cells (Liu *et al.*, 2014). Blebbistatin plus lamin-A knockdown combined did not further decrease the apparent nuclear stiffness in the MSCs,

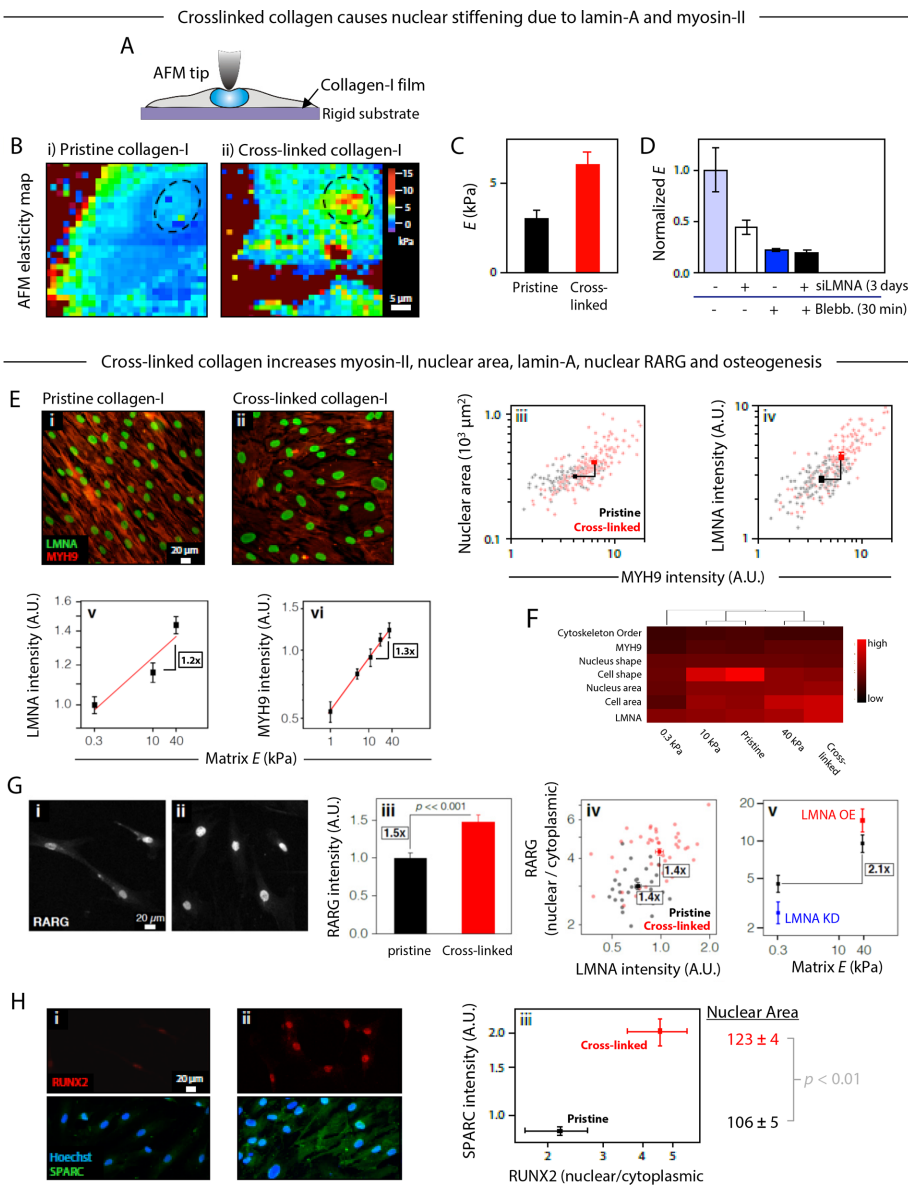


FIGURE 4: Influence of matrix mechanics on osteogenic pathways: effect of collagen cross-linking on nuclear elasticity and protein expression. (A) AFM was used to probe the stiffness profiles of MSCs cultured on a rigid substrate, thus allowing an in situ readout of cellular elasticity without having to deconvolute effects of substrate deformation. (B) Force–volume mode elasticity maps of living cells cultured for 6 d on (i) pristine and (ii) cross-linked collagen-1 films, showing that matrix cross-linking caused a twofold increase in the Young's modulus of the nuclear region (dashed circles). (C) Young's moduli obtained from force–indentation curves at the position of the nucleus, averaged from ~60 curves/cell and 7–13 individual/sample, cultured on pristine or cross-linked collagen films. (D) Relative contributions to the normalized stiffness of the nuclear region from the nuclear lamina and cortical tension in the actomyosin network can be appreciated by treatments with small interfering LMNA (siLMNA) and blebbistatin, respectively (averaged from ~60 force–indentation curves measured at different locations within the nuclear region of four to seven cells cultured on plastic). (E) MSCs cultured for 2 wk on cross-linked collagen-1 films have 1.5-fold higher levels of LMNA. Immunofluorescence images of LMNA (green) and myosin-IIA (MYH9, red) on (i) pristine and (ii) cross-linked collagen-1 films. Quantitative image analysis showed that (iii) increased levels of MYH9 correlated with greater nuclear spread area and (iv) higher levels of LMNA ($n > 115$ cells; significantly different in both dimensions, $p < 0.01$). (v, vi) LMNA and MYH9 levels in MSCs on gels shown for comparison. (F) Heat map summary and hierarchical clustering of cellular and nuclear parameters, as well as protein expression, on 0.3-, 10-, and 40-kPa gels and both pristine and cross-linked collagen films from various experiments. The dendrogram indicates that cells on 10-kPa gels and pristine films cluster together, as do cells on 40-kPa gels and cross-linked films, whereas cells on soft, 0.3-kPa gels are distinct from the others. (v) LMNA intensity on gels. (vi) MYH9 intensity on gels. (G) Comparison of the cellular

probably because 1) blebbistatin alone tends to quickly decrease lamin-A levels (Buxboim *et al.*, 2014), and 2) lamin-A knockdown alone reduces the levels of myosin-II in MSCs over days through the serum response factor (SRF) pathway (Ho *et al.*, 2013; Swift *et al.*, 2013b; Buxboim *et al.*, 2014; Talwar *et al.*, 2014). In other words, endogenous lamin-A, contractility, and nuclear stiffness are all mechanically linked—at least in these cells.

MSCs expressing ectopic green fluorescent protein (GFP)–lamin-A (Supplemental Figure S3A) had an apparent nuclear stiffness (on cross-linked nanofilms) that increased with GFP-lamin-A level. To eliminate contributions of the cytoskeleton, MSCs were detached, the actomyosin cytoskeleton was depolymerized with latrunculin, and micropipette aspiration was used to measure nuclear stiffness in suspended cells. The results demonstrate increased nuclear stiffness with GFP–lamin-A independent of cytoskeleton (Supplemental Figure S3B). Nonetheless, time-dependent changes in apparent nuclear stiffness over 2 wk in culture on cross-linked nanofilms (Supplemental Figure S3C) are likely a result of changes in both lamin-A levels and actomyosin tension.

For MSCs cultured on pristine or cross-linked films, immunofluorescence analyses of lamin-A nuclear area and myosin-IIA in single cells at 2 wk (Figure 4E, i and ii) generally revealed that LMNA correlated with increased nuclear spreading and levels of MYH9 (Figure 4E, iii and iv). Of importance, collagen cross-linking caused a 1.5-fold

location of transcription factor RARG in MSCs cultured on (i) pristine and (ii) cross-linked collagen-1 films. (iii) A quantification of RARG levels showed a significant increase on cross-linked substrate ($n > 50$ cells). (iv) A cell-by-cell analysis showed that cross-linked collagen films favor higher LMNA and a correlated increase in the nuclear-to-cytoplasmic ratio of RARG ($n > 30$ cells; significantly different in both dimensions, $p < 0.01$). (v) Average nuclear-to-cytoplasmic ratio of RARG on gels. (H) RUNX2 and SPARC were also compared in MSCs cultured on (i) pristine and (ii) cross-linked collagen-1 films. Quantification of the images (iii, correlating results from two separate experiments) showed that cross-linked substrates favored a greater nuclear localization of transcription factor RUNX2 and a greater expression of osteogenic marker SPARC. Nuclear spread area is also highest on cross-linked films, as predicted from the fits of Figure 3D i. All experiments, $n \geq 3$ (mean + SEM).

average increase in LMNA, which is consistent with observations of MSCs on soft versus stiff gels (Figure 4E, v and vi; Swift *et al.*, 2013b; Buxboim *et al.*, 2014). Scatter plots for all of these single-cell analyses always show that some cells on the cross-linked films fall within the response envelopes of cells on pristine films, so that this shared subpopulation of nonresponding cells at least provides a common basis for extrapolation of the trend. A heat map of quantified morphologies and protein levels in MSCs on the nanofilms and gels of varied stiffness (Figure 4F) clusters together the cell phenotype on pristine films with that on 10-kPa gels and separately clusters together the cell phenotype on cross-linked films with that on 40-kPa gels, whereas cell phenotypes on soft gels are most distinct. Compared to similar analyses of transcriptomes, this direct alignment of cell phenotypes is likelier to reflect mechanosensitive processes such as protein degradation that sometimes decouple from transcript levels (Dingal *et al.*, 2015).

Immunostaining for the transcription factor RARG, which generally correlates with lamin-A in tissues (Figure 2C) and can in principle regulate *LMNA* transcription (Swift *et al.*, 2013b), showed that the total amount of RARG increased on cross-linked films after just 2 d in culture (Figure 4G, i–iii). RARG's nuclear-to-cytoplasmic ratio in cells on nanofilms also correlated with lamin-A intensity in a cell-by-cell analysis, which is in good agreement with similar trends for cells on gels (Figure 4G, iv and v). Mechanistic links are supported here later by short-time kinetic studies that use soluble RA ligand.

Based on the surprisingly general association between collagen cross-linking and levels of key osteogenic factors (Figure 2C), MSCs on the two types of nanofilms were assessed for osteoinduction without addition of any osteogenic soluble factors. RUNX2 is an early osteogenic transcription factor required for osteogenesis (Choi *et al.*, 2001); RUNX2 was mostly nuclear after 1 wk in culture and greater than twofold more so on cross-linked nanofilms (Figure 4H). The results are consistent with matrix elasticity-directed lineage specification on stiff gels even in the absence of “osteoinduction media” (Engler *et al.*, 2006; Benoit *et al.*, 2008; Chen *et al.*, 2010). SPARC (or osteonectin) is a late marker of osteogenesis and is a bone glycoprotein secreted by osteoblasts to initiate mineralization (Terminet *et al.*, 1981); SPARC was also greater than twofold higher after 2 wk on cross-linked films. Nuclei in the more osteogenic state were more spread ($p < 0.01$), which once again suggests higher cytoskeletal tension on the stiffer matrix. The findings thus suggest that 1) the stiffness of cross-linked nanofilms is osteoinductive, and 2) stiffness sensing might be amplified by coupling to soluble factor regulation of the increased nuclear RARG.

RARG antagonist and agonist respectively increase/maintain or decrease LMNA and progerin only on stiff substrates

RA signaling pathways affect many developmental and homeostatic processes. We previously found that the pan-RAR antagonist AGN (AGN193109; Supplemental Figure S4A) enhances osteogenesis of MSCs cultured in osteoinduction medium (OIM; Swift *et al.*, 2013b). RARG-specific agonists slow ectopic bone growth in mouse models (Shimono *et al.*, 2012), but antagonists have been unexplored. Here we tested antagonists or agonists that are more specific to RARG (Supplemental Figure S4A), and for a wider range of MSCs, we first measured the effects on LMNA levels. Whereas agonists tended to decrease LMNA, antagonists tended to increase LMNA on standard rigid culture plastic (Figure 5A). To clarify the trend on various stiff or rigid substrates, we tabulated the (antagonist/agonist) effect on LMNA across primary MSCs for various drug pairs and found 1.8 ± 0.2 for the mean ratio (\pm SEM; Figure 5B and Supplemental Figure S4B). Donor variability of MSCs is at least one source of variation.

The iPSCs can be a more uniform source of MSCs that turn on expression of lamin-A with loss of pluripotency (Zhang *et al.*, 2011; Talwar *et al.*, 2013). The iPSC-MSCs also have no memory of the many factors in a bone marrow niche. Application of retinoids to iPSC-MSCs gave (antagonist/agonist) effects on LMNA levels that were statistically the same as for primary bone marrow MSCs (Figure 5B). Of importance, progeria patient-derived iPSC-MSCs showed similar effects on lamin-A levels with both RARG-specific and -non-specific drugs (Figure 5C and Supplemental Figure S5F). Although progerin is a mutated form of lamin-A protein that causes accelerated aging, expression of the progerin allele should be unaffected. Immunoblots showed the drugs affect progerin from the disease-causing allele as much as the normal lamin-A splice-forms (Figure 5C, bottom, and Supplemental Figure S5E). Retinoid effects are strong in early passages when cultured on rigid substrates, where the nucleus is well spread (Supplemental Figure S5C). Agonist treatment also resulted in an ~40% increase of nuclei with irregular shapes and showed LMNA enrichment in high-curvature regions (tips; Supplemental Figure S5D). Previous studies with other cell types showed that increased progerin results in misshapen nuclei (Goldman *et al.*, 2004), but cytoskeletal forces in the MSCs studied here could have different effects on nuclei. For all of the different MSCs tested, the findings are nonetheless consistent with retinoids contributing to transcriptional control of *LMNA*.

To test the functional consequences of the low nuclear RARG seen in MSCs on pristine collagen nanofilms (Figure 4F), we compared the RARG-specific antagonist CD2665 with the RARG-specific agonist CD1530 in terms of effects on LMNA in MSCs on the two types of nanofilms. The cross-linked nanofilm produced the expected LMNA ratio for antagonist/agonist, but the pristine nanofilm, which was soft (Figure 3, D and E), gave no significant retinoid effects (Figure 5D). Lamin-A levels were nonetheless highest in MSCs on cross-linked nanofilms, consistent with Figure 4E. For insight into the kinetics of the effect of the RARG-specific antagonist CD2665, we treated MSCs on a rigid substrate with drug and imaged them. Within 40 min, nuclear localization of RARG increased (by ~15%; $p = 0.05$) and remained high, whereas LMNA required 4 h to be significantly higher (Supplemental Figure S4C). Taken together, these findings suggest fast-acting cooperation between soluble factor and mechanosensitive pathways.

To assess the retinoid responsiveness in cooperation with matrix stiffness, we examined how lamin-A level depends on nuclear area when treated with RA agonist/antagonist. First, we established the reversibility of nuclear spreading: iPSCs were induced to differentiate into MSCs with well-spread cells and nuclei on gelatin-coated plastic (which is rigid with $E > 100$ kPa based on AFM measurements), but replating onto soft gels (2 kPa) caused a decrease in both nuclear area and its variation (Figure 5E). Parallel analyses of distributions for Lamin-A as well as nuclear area revealed a “weak-responder” subpopulation of cells on stiff gels that respond like 95% of cells on soft gels. About one-third of cells sense the stiffness and spread with high lamin-A, and retinoids affect an equal fraction (32–36%) in regulating lamin-A levels (Figure 5Fi). The same proved true for bone marrow-derived MSCs on pristine and cross-linked films. Of importance, retinoids have no effect on nuclear translocation of RARG in cells on either film, even though the cross-linked matrix drives more RARG into the nucleus and lamin-A decreases with agonist while increasing slightly with antagonist (Figure 5Fii).

A parsimonious dynamical model of the mechanochemical effects on the *LMNA* gene circuit was developed to fit the data (Figure 6A). We incorporated the finding that lamin-A protein is stabilized by cytoskeletal stresses on stiff matrices (Dingal and Discher, 2015). Similar

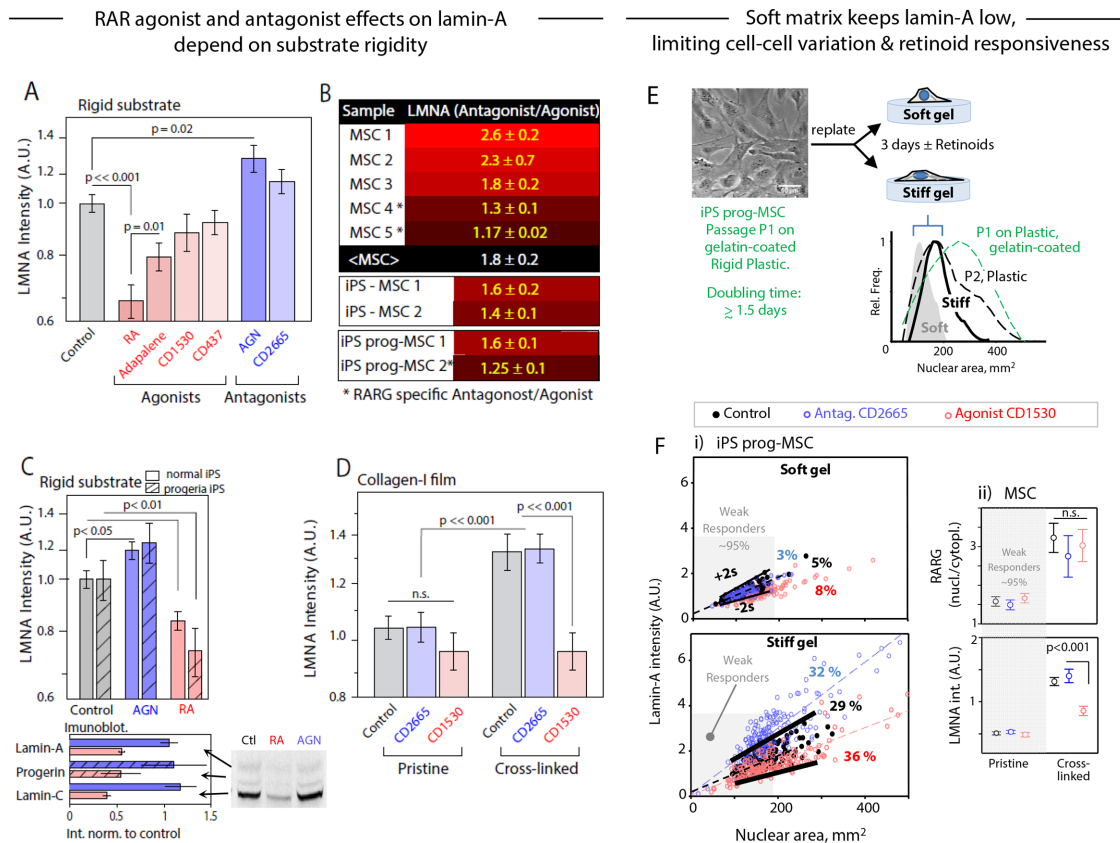


FIGURE 5: Influence of soluble factors on RA pathway implicated in osteogenesis: convergence of mechanochemical effects. (A) MSCs cultured on plastic with drugs that perturb the RA pathway (control is ethanol/dimethyl sulfoxide vehicle only; drug treatments at 1 μM , except adapalene and CD437 at 0.1 μM ; see Supplemental Figure S4A for summary of drug properties). LMNA was quantified by immunostaining after 4 d. (B) Although the magnitude of response varied across MSCs from different donors, RA pathway antagonists consistently increased LMNA level with respect to the agonist on a range of stiff substrates (rigid plastic, stiff polyacrylamide gels, collagen thin films; see Supplemental Figure S4B for full table); iPS-derived MSCs and progeria patient-derived iPS-MSCs gave similar response (bottom of the table). (C) Antagonist/agonist effects on LMNA levels from immunofluorescence of iPS-MSCs and progeria patient-derived iPS-MSCs relative to control. The immunoblots (bottom) showed that the progerin from the disease-causing allele was affected as much as the normal lamin-A spliceforms. (D) LMNA was quantified by immunofluorescence in MSCs treated for 3 d with RARG-specific RA pathway antagonist CD2665 or agonist CD1530 while being cultured on pristine or cross-linked collagen-I films. Consistent with earlier reports (Swift *et al.*, 2013b), a significant differential response between agonist and antagonist is apparent only on a “stiff” (cross-linked) substrate. (E) (i) The spread area of nuclei in iPS-progeria-derived MSCs depends on matrix stiffness and is reversible. Early passage, P1, MSCs spread less as P2 on soft gels than on stiff gels or plastic. (F) Nuclear area and lamin-A in iPS-progeria-derived MSCs on soft gels of 2 kPa shows that 95% of cells are within $\pm 2\sigma$ of untreated cells even after treatment with RA agonist/antagonist. These cells are “weak responders” to retinoids, and the same range of small nuclear areas identifies weak responders to retinoids on stiff gels of 50 kPa. However, about one-third of cells are mechanosensitive to stiffness, with elevated lamin-A levels that also change in response to retinoids. (ii) Nuclear RARG in bone marrow-derived MSCs on pristine and cross-linked films increases (for responding cells) with matrix stiffness, but retinoids have no effect on RARG, even though lamin-A tends to decrease with agonist and increase with antagonist.

models have been developed for cytoskeletal regulation of SRF genes (Jain *et al.*, 2013). Soluble factor effects on RARG translocation for *LMNA* transcription were incorporated (Figure 6A), and variation of antagonist/agonist effects on lamin-A levels (e.g., cell-to-cell variation) were emulated by varying the relative strength of RARG-antagonist/agonist binding to the *LMNA* promoter (Figures 5B and 6B). In particular, increased binding sensitivities (lower k_s) increased the modulation by soluble factors of *LMNA*. This matrix-modulated noise analysis appears novel and might imply that for individual cells that start more stem-like and less osteogenic, soluble-factor induction of *LMNA* via RARG is most effective. A matrix elasticity-dependent nuclear localization of RARG (r_{nucl}) was also necessary to capture soluble-

factor effects on lamin-A levels (Figures 5C and 6C). The model predicted not only the orthogonality of purely mechanical and purely chemical pathways but also that the combination synergizes to maximally regulate levels of lamin-A protein (Figure 6D).

RARG antagonist and agonist respectively increase and decrease osteogenesis in vitro and in vivo

To assess functional effects of retinoids on osteogenesis, we assayed ALP activity as a first readout for osteoinduced MSCs cultured with OIM on rigid substrates. The RARG-specific antagonist CD2665 showed the greatest effect in enhancing ALP staining of cultures, by ~12-fold relative to osteoinduced MSC controls not treated with

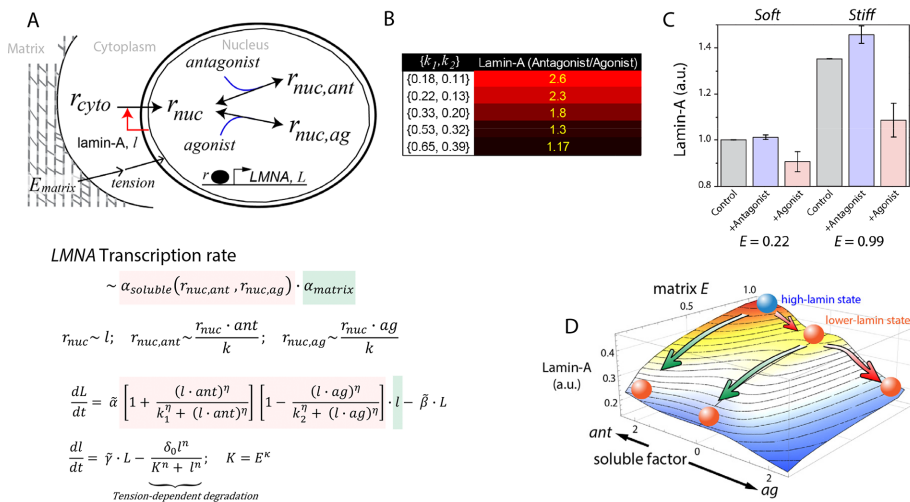


FIGURE 6: Waddington-inspired model of mechanochemical effects on lamin-A levels. (A) Lamin-A (l) levels increase with matrix elasticity (E_{matrix}) and influence cytoplasmic RARG (r_{cyto}) shuttling into the nucleus (r_{nuc}), where its binding on LMNA (L) promoter as a repressor can be enhanced or abrogated by soluble agonist (ag) or antagonist (ant). Transcription rate of LMNA is a function of both soluble (α_{soluble}) and matrix (α_{matrix}) factors. Soluble effects are, in turn, modulated by the levels of RARG-antagonist ($r_{\text{nuc,ant}}$) and RARG-agonist ($r_{\text{nuc,ag}}$) complexes, whose dissociation constants are represented by k_1 and k_2 , respectively. Building from our previous model, in which lamin-A's tension-inhibited degradation, K , is key to its scaling with matrix elasticity, E , we extended the model to capture the convergence of mechanical and chemical effects on lamin-A. Model parameters were specified by recapitulating experimental results in Figure 5, B and D: $\tilde{\alpha} = 0.35$; $\tilde{\beta} = 3$; $\tilde{\gamma} = 1$; $\delta_0 = 2.5$; $\eta = 4$; $k_1 = 0.5$; $k_2 = 0.3$; $n = 4$; $\kappa = 0.6$. (B) Sensitivity analysis of varying binding strengths of RARG antagonist (k_1) or agonist (k_2) complexes to lamin-A expression response ($E = 0.99$, {ant, ag} = {1,0} or {0,1}). (C) For pristine (relative $E = 0.22$) and cross-linked (relative $E = 0.99$) films, antagonist (ant) and agonist (ag) values were set to 1.0. Error bars are SDs derived from simulating 100 cells with k_1 and k_2 randomly generated as values within the ranges [0.4, 0.6] and [0.2, 0.4], respectively. (D) The model predicts two paths from a high-lamin state (blue sphere) to low lamin-A states (red spheres) by reducing matrix E (green arrows) or adding soluble agonist (red arrows). All experiments, $n \geq 3$ (mean + SEM).

retinoids. CD2665s effect was also 50% greater than that of the pan-RAR antagonist AGN. Of importance, LMNA knockdown decreased ALP nearly to control levels for the antagonists (Figure 7, A and B). Agonists that were either RARG-specific (CD1530) or pan-RAR (RA) tended to decrease ALP but with little effect of LMNA knockdown. With the RARG-specific antagonist CD2665, single-cell analyses show that LMNA^{high} cells are sixfold more likely to also be ALP^{high} than LMNA^{low} cells, and the supermajority of cells (62%) are both ALP^{high} and LMNA^{high} (Figure 7C). Knockdown of LMNA increases the ALP^{low} subpopulations by greater than fivefold despite the presence of antagonist. Although retinoids can affect many pathways, given their demonstrated influence on lamin-A levels (e.g., Figure 5; via promoter-based transcriptional regulation (Okumura et al., 2004)), and given the evidence that nuclear accumulation of RARG is favored by LMNA^{high} (e.g., Figure 4G), it is fully consistent to find that differentiation also exhibits synergy between RARG-specific soluble factors and matrix rigidity.

To provide further evidence that the RARG-specific antagonist CD2665 promotes osteogenesis, MSCs were pretreated with drug (or not) for 3 d, implanted into mouse flank for 2–3 mo per Figure 2A, and then analyzed for calcification. With live mice, fluorescent bisphosphonate was injected and imaged, revealing a bone-like intensity for CD2665-treated xenografts that was significantly greater than controls (Supplemental Figure S6, B and C). Xenograft tissue was removed and stained with alizarin red for calcification. Antago-

nist gave a calcification signal similar to bone, which is threefold to fourfold greater than xenografts from either untreated control or agonist pretreated MSCs (Figure 7D). ALP staining showed similar trends for the xenografts (Supplemental Figure S6E). The RARG-specific antagonist thus promotes osteogenesis in vitro and in vivo.

Convergent overlap in synergistic differentiation

Although cell-to-cell variation can be large (Figure 7C), robustness of differentiation in noisy systems can be achieved through parallel systems of feedback (Ahrends et al., 2014). Proteomic changes were therefore compared between MSCs treated with AGN versus RA, as characteristic of the soluble factor input, and control versus LMNA knockdown. Based on detection of three or more tryptic peptides per protein, 21 proteins (of 121 quantified) varied by >1.33-fold in both experiments (Supplemental Figure S7A), and most exhibited correlated responses to both perturbations (Figure 7E). Given the wide-ranging studies of retinoids that rarely if ever mention lamin-A, it seems unsurprising that most pathways regulated by retinoids differ from those affected by lamin-A; this makes their interplay in differentiation that much more biologically significant. Gene ontology and literature analyses of the 21 overlapping proteins nonetheless identified a number of molecules relevant to synergy in osteogenic processes (Figure 7F), particularly STAT1, MYO1B, and PDIA3 (Miyashita et al., 1998; Balmer and Blomhoff,

2002; Xiao et al., 2004; Tajima et al., 2010; Wang et al., 2010; Roosa et al., 2011; Gao et al., 2012). Further comparison to transcriptional changes after LMNA knockdown suggested additional overlap candidates while adding confidence to common factors STAT1, ALCAM, EHD2, MVP, and P4HA2 (Figure 7G and Supplemental Figure S7B).

DISCUSSION

Collagen cross-linking, stiffer tissues, and stiffer nucleus

A cell might respond to the rigidity of a single matrix fibril that integrins bind (Watt and Huck, 2013), or it might respond to collective matrix properties at a larger scale. Stress-bearing bone, cartilage, and muscle must all have sufficient strength and stiffness at a macroscopic scale to sustain the large forces of tissue function (e.g., walking). However, the microenvironment with which bone-making osteoblasts interact is collagen rich and not calcified (Sodek and McKee, 2000), which should make this osteoid much softer than the large-scale properties of rigid bone. MSCs that enter such an osteogenic niche from marrow (such as perivascular niches; Park et al., 2012) transit from a very soft marrow niche to a stiff but thin collagenous niche, for which the novel nanoscale measurements here indicate is softer than bone (Figure 1). Osteoid is reasonably approximated in terms of cell-perceived stiffness (Figure 3) by a cross-linked collagen-I nanofilm, which is more osteogenic for MSCs than a pristine collagen-I nanofilm (Figure 4). Broader significance is suggested by meta-analysis of transcriptomes across many tissues

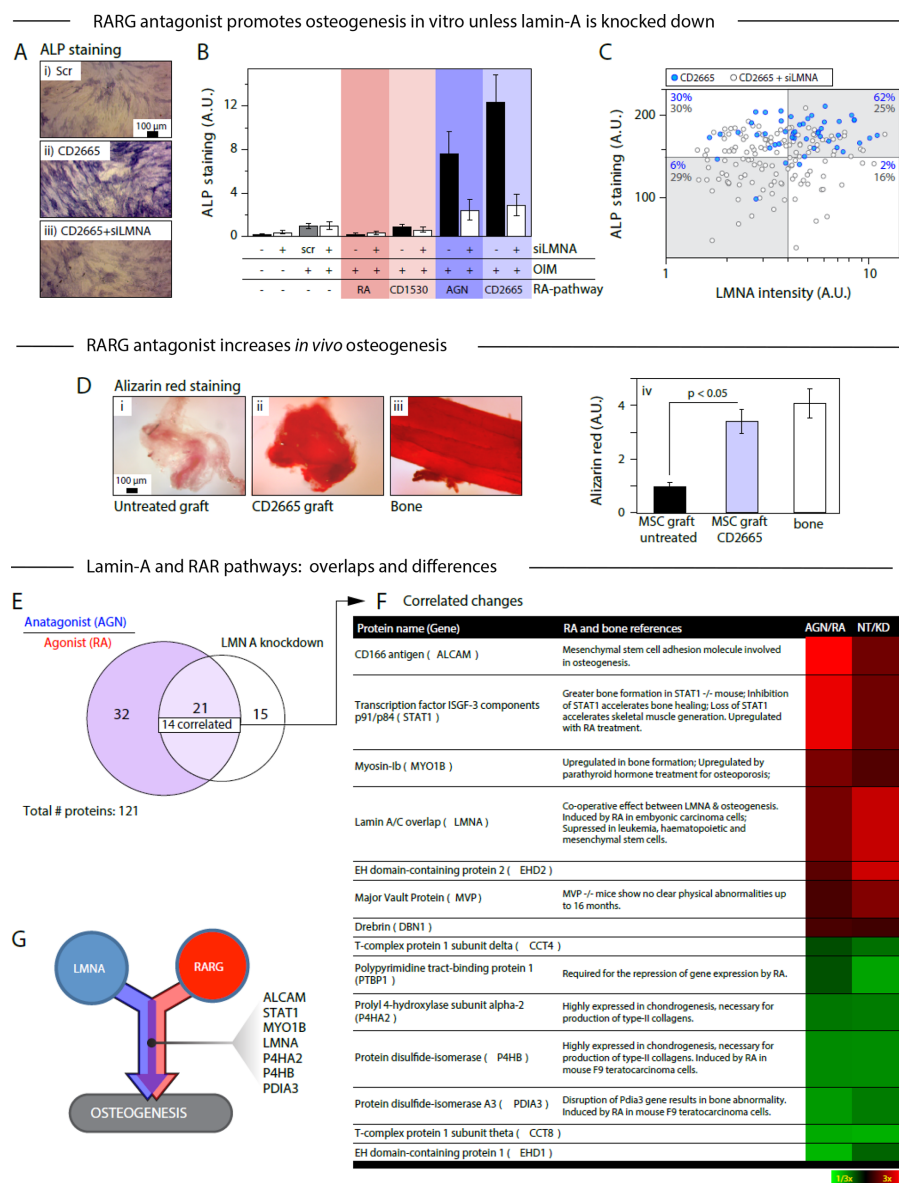


FIGURE 7: Proteomic comparison of the effects of LMNA knockdown and drug perturbations to the RA pathway allows identification of factors common to both pathways. (A) MSCs were cultured on plastic for 1 wk with combinations of OIM, siLMNA, and drug perturbations to the RA pathway. (i) ALP staining of scrambled RNA and OIM. (ii) RARG-specific antagonists CD2665 and OIM. (iii) siLMNA, CD2665, and OIM. (B) ALP activity is enhanced in the presence of RA antagonists, but this effect is abrogated by LMNA knockdown. (C) A cell-by-cell analysis of LMNA level correlated with local ALP staining in MSCs cultured on rigid substrate with OIM and CD2665, with or without siLMNA, showed that higher LMNA levels positively correlate with greater osteogenesis (Supplemental Figure S5A). The percentages indicate the number of points (blue, without siLMNA; gray, with siLMNA) in quadrants defined by the means of the siLMNA points. (D) Antagonist to RARG also increased osteogenesis *in vivo*: MSCs were grafted into mouse flank, excised after 4 wk, and stained with alizarin red, an indicator of osteogenic calcification: (i) untreated MSC graft; (ii) CD2665 pretreated MSC graft; (iii) mouse femur; (iv) quantification of staining. These experiments done in duplicate suggest that CD2665 pretreatment increased the bone-like character of the grafted MSCs (Supplemental Figure S5, B and D). (E) MSCs were cultured on plastic for 8 d with drug perturbation to the RA pathway or subjected to LMNA knockdown. Cells were analyzed by MS proteomics: of 121 proteins quantified (with more than three peptides per protein), 53 varied by >4/3-fold in the RA-perturbation experiment, and 36 varied by the same degree in the siLMNA experiment (Supplemental Figure S6A). Twenty-one proteins varied in both experiments, and of these, 14 were positively correlated. (F) Table of correlated protein changes with a heat map representation of fold change in RA pathway and siLMNA experiments. See Supplemental Figure S7 for references. (G) Representation of proteins involved with overlapping pathways to osteogenesis. Unless indicated, $n \geq 3$ (mean + SEM).

(excluding bone; Figure 2), with potential relationships emerging between cross-linked collagen, lamin-A, which confers nuclear stiffness, and RARG, which can in principle regulate lamin-A transcription (Swift *et al.*, 2013b) and even osteoinduction. The latter might lend insight into ectopic calcification that is sometimes seen after injury coincident with scars having an abundance of collagen that is highly cross-linked (Shimono *et al.*, 2012). However, the response of lamin-A to matrix rigidity appears more general and can occur even within hours (Supplemental Figure S4; Buxboim *et al.*, 2014), but whether RARG and downstream pathways are independent or synergize for differentiation is key to understanding signals in a niche.

With cross-linked collagen-I, if a cell adheres to and pulls on even one fibril, bending of that fibril will also require bending of adjacent fibers (Figure 3), which means that the cell should feel a stiff film. With synthetic gels that are also modified with adhesive ligands such as collagen, molecular-scale mechanisms of force transmission remain unclear (Watt and Huck, 2013). Nonetheless, gel stiffness generally drives cell spreading, which requires actomyosin stress fiber formation (Discher *et al.*, 2005), and the MSC nucleus also becomes more spread and flattened, with lamin-A levels increasing while B-type lamins are unchanged (Supplemental Figure S2, F and G). Cross-linked collagen-I films and stiff gels cause similar MSC responses (Figure 3), but only the cross-linked nanofilms on rigid mica permit probing of nuclear stiffness (as opposed to indenting nuclei into gels beneath a cell), helping to show that nuclear stiffening parallels matrix stiffening (Figure 4). Nuclear stiffening's dependence on lamin-A and actomyosin is consistent with the pathway for lamin-A accumulation in MSCs on stiff substrates: actomyosin tension opposes lamin-A phosphorylation and degradation that occurs in cells on soft gels (Buxboim *et al.*, 2014). Downstream pathways are reasonably clear because we previously showed (Swift *et al.*, 2013b) that the lamin-A-binding protein SUN2 coimmunoprecipitates with RARG and that overexpressed SUN2 decreases both nuclear RARG and lamin-A. We can therefore infer that high lamin-A levels favor nuclear retention of SUN2 and RARG, which primes the latter for transcriptional control of LMNA. Consistent with these aspects of mechanism worked out with cells on gels, cross-linked nanofilms here indeed increase nuclear RARG relative to MSCs on pristine films (Figure 4), and addition of

RARG-specific antagonist increases nuclear accumulation of RARG and lamin-A levels within hours (Supplemental Figure S4). Whereas pan-RAR agonists and antagonists suggest roles for RARs (Switt *et al.*, 2013b), RARG-specific agonists and antagonists provide functional evidence for this isoform distinct from RARA and RARB (Figure 5 and Supplemental Figure S4). Our calculations for the mechanochemical gene circuit thus couple matrix elasticity regulation of lamin-A protein to effects of RARG soluble factor on lamin-A expression. Of importance, RARG antagonist/agonists are ineffective on MSCs on soft matrix according to both experiments and calculations (Figure 5).

Implications for progerin and aging

Microenvironments trigger and direct stem cell differentiation, but microenvironments can change in aging, and so can lamin-A. For example, collagen-I-rich skin (Figure 2A) stiffens twofold to threefold in human aging (Diridollou, 2001), and progerin, in addition to normal lamin-A, has been detected in skin biopsies and fibroblasts of normal donors >80 yr of age (Dahl *et al.*, 2006; McClintock *et al.*, 2007). The potential rejuvenating effects of RA on aging tissues such as skin has many complexities (Mukherjee *et al.*, 2006), and the results here for progerin, as well as normal lamin-A (Figure 5B and Supplemental Figure S5), suggest additional complexity because such soluble factors are generally applied to cells adhering to matrix or another cell that can influence cell responses as extreme as differentiation. Furthermore, RAR antagonists might naturally derive from vitamin A (Eroglu *et al.*, 2012), as is the case for RA, and so the antagonist/agonist balance or imbalance in a given microenvironment or niche could contribute to levels of both normal lamin-A and progerin. Levels can have a dramatic effect on health: homozygous lamin-A-knockout mice all die 3 wk postpartum with major heart and cardiovascular defects (similar to progerin mice that die), whereas heterozygotes maintain normal heart function at least 20-fold longer (Kubben *et al.*, 2011). Beyond retinoids and lamins, responses of cells on rigid coverslip glass or tissue culture plastic to other drugs that converge on mechanosensitive pathways could be different from those of the same cells on soft, tissue-like matrix.

Translatable potential versus matrix-associated growth factors

Matrix-associated growth factors such as transforming growth factor β superfamily members have potent effects on stem cells, including effects of bone morphogenetic protein 2 (BMP 2) on bone formation (e.g., Hayashi *et al.*, 2009). However, the release of such matrix-bound factors depends in part on matrix mechanics and cell contractility (Wipff *et al.*, 2007), which of course tie such factors to matrix pathways that are distinct from purely soluble factors such as retinoids (Figure 1A). Implants that are simply loaded with recombinant human BMP cause ectopic bone (Carragee *et al.*, 2011). RARG antagonist pretreatment of human bone marrow MSCs leads to human bone formation *in vivo* even without addition of BMPs (Figure 7D) and could prove a useful alternative for bone tissue engineering. Of importance, whereas matrix inputs might only affect cells while they are in contact with matrix (Schellenberg *et al.*, 2014), short periods of soluble factor pretreatment of stem cells can have long-term effects such as *in vivo* osteogenesis over many weeks. Retinoids can certainly drive epigenetic programs (Gudas, 2013), and matrix mechanics could exert similar effects, especially given the mechanosensitivity of lamin-A.

MATERIALS AND METHODS

AFM on primary tissue and cells on films

Tissue samples or mica disks with cultured cells were attached to a glass dish fully immersed in medium at 37°C and indented with soft cantilevers with nominal spring constants of 0.01 N/m when probing bone marrow or 0.05 N/m for osteoid and cells. Before each experiment, cantilevers were calibrated using a thermal fluctuations method. The distribution of Young's modulus of bone tissues was evaluated from measurements at multiple locations in tibia samples from six different mice. Silverman's test (Silverman, 1981) for multimodality in R package "silvermantest" (www.uni-marburg.de/fb12/kooperationen/stoch/forschung/rpackages) was used with a null hypothesis that the logarithm of the data has at most two modes. The *p* value of the test was <0.01, which provides strong statistical evidence for at least three modes. The Sneddon modification to the Hertz model for a conical tip was used to calculate the apparent Young's modulus, assuming indentations to an isotropic, homogeneous material. The depth of indentations was determined using the procedure in Buxboim *et al.* (2010); it is between 400 nm and 1 μ m, and the fitting range was obtained by minimizing the fitting error assuming a Poisson ratio of 0.5. All measurements were performed within hours of mouse killing in order to preserve the *in vivo* properties of the tissue. Cells on collagen films were probed in force-volume mode with a resolution of 128 \times 128 indentation curves per frame, with a scanning frequency of 0.2 Hz. Topographical images of fixed cells were taken in contact mode.

Preparation of thin collagen films

Rat-tail collagen solution (CB354249; Corning; 200 μ l at 1 μ g/ml in 50 mM glycine buffer, 200 mM KCl, pH 9.2) was deposited on freshly cleaved mica disks at room temperature for self-assembly. After 30 min, liquid was gently aspirated, and disks were washed with Dulbecco's phosphate buffered saline (DPBS). The collagen films were cross-linked with tissue transglutaminase (T5398; Sigma-Aldrich; concentration 30 μ g/ml in 50 mM Tris buffer, 5 mM CaCl₂, and 2 mM dithiothreitol at pH 7.4). The films were immersed in the solution and agitated for 4 h at 37°C before washing with DPBS.

AFM of thin films

Collagen films were imaged in DPBS at room temperature in tapping mode with driving frequency close to the resonance frequency of the cantilever. Fibril deformation was performed in a direction perpendicular to the fibril orientation in contact mode with predefined force and trajectory. After scratching, films were reimaged in tapping mode.

ACKNOWLEDGMENTS

We thank the Wistar Institute Proteomics Core for MS support, D. Gilbert (Florida State University) for GFP-lamin-A, and A. Miyawaki (RIKEN) for the genetically encoded probe for RA, GEPR. We were supported by National Institutes of Health/National Cancer Institute PSOC Award U54 CA193417, National Heart Lung and Blood Institute Awards R01 HL124106 and R21 HL128187, a National Science Foundation Materials Science and Engineering Center grant to the University of Pennsylvania, the US-Israel Binational Science Foundation, and Charles Kaufman Foundation Award KA2015-79197. The content of this article is solely the responsibility of the authors and does not necessarily represent the official views of the National Institutes of Health or other granting agencies.

REFERENCES

- Ahrends R, Ota A, Kovary KM, Kudo T, Park BO, Teruel MN (2014). Controlling low rates of cell differentiation through noise and ultrahigh feedback. *Science* 344, 1384–1389.
- Alexander B, Daulton TL, Genin GM, Lipner J, Pasteris JD, Wopenka B, Thomopoulos S (2012). The nanometre-scale physiology of bone: steric modelling and scanning transmission electron microscopy of collagen-mineral structure. *J R Soc Interface* 9, 1774–1786.
- Al-Jallad HF, Nakano Y, Chen JLY, McMillan E, Lefebvre C, Kaartinen MT (2006). Transglutaminase activity regulates osteoblast differentiation and matrix mineralization in MOT3-E1 osteoblast cultures. *Matrix Biol* 25, 135–148.
- Balmer JE, Blomhoff R (2002). Gene expression regulation by retinoic acid. *J Lipid Res* 43, 1773–1808.
- Benoit DSW, Schwartz MP, Durney AR, Anseth KS (2008). Small functional groups for controlled differentiation of hydrogel-encapsulated human mesenchymal stem cells. *Nat Mater* 7, 816–823.
- Bridger JM, Foeger N, Kill IR, Herrmann H (2007). The nuclear lamina—a structural framework and a platform for genome organization. *FEBS J* 274, 1354–1361.
- Buxboim A, Rajagopal K, Brown AEX, Discher DE (2010). How deeply cells feel: methods for thin gels. *J Phys Condens Matter* 22, 194116.
- Buxboim A, Swift J, Irianto J, Athirasala A, Kao Y-RC, Spinler KR, Dingal PCDP, Discher DE (2014). Matrix elasticity regulates lamin-A,C phosphorylation and turnover with feedback to actomyosin. *Curr Biol* 24, 1909–1917.
- Carragee EJ, Hurwitz EL, Weiner BK (2011). A critical review of recombinant human bone morphogenetic protein-2 trials in spinal surgery: emerging safety concerns and lessons learned. *Spine J* 11, 471–491.
- Chen WLK, Likhitpanichkul M, Ho A, Simmons CA (2010). Integration of statistical modeling and high-content microscopy to systematically investigate cell-substrate interactions. *Biomaterials* 31, 2489–2497.
- Choi JY, Pratap J, Javed A, Zaidi SK, Xing LP, Balint E, Dalamangas S, Boyce B, van Wijnen AJ, Lian JB, et al. (2001). Subnuclear targeting of Runx/Cbfa/AML factors is essential for tissue-specific differentiation during embryonic development. *Proc Natl Acad Sci USA* 98, 8650–8655.
- Cisneros DA, Friedrichs J, Taubenberger A, Franz CM, Muller DJ (2007). Creating ultrathin nanoscopic collagen matrices for biological and biotechnological applications. *Small* 3, 956–963.
- Cox TR, Bird D, Baker AM, Barker HE, Ho MWY, Lang G, Erler JT (2013). LOX-mediated collagen crosslinking is responsible for fibrosis-enhanced metastasis. *Cancer Res* 73, 1721–1732.
- Dahl KN, Scaffidi P, Islam MF, Yodh AG, Wilson KL, Misteli T (2006). Distinct structural and mechanical properties of the nuclear lamina in Hutchinson-Gilford progeria syndrome. *Proc Natl Acad Sci USA* 103, 10271–10276.
- Darling EM, Topel M, Zauscher S, Vail TP, Guilak F (2008). Viscoelastic properties of human mesenchymally-derived stem cells and primary osteoblasts, chondrocytes, adipocytes. *J Biomech* 41, 454–464.
- Dingal P, Bradshaw AM, Cho S, Raab M, Buxboim A, Swift J, Discher DE (2015). Fractal heterogeneity in minimal matrix models of scars modulates stiff-niche stem-cell responses via nuclear exit of a mechanorepressor. *Nat Mater* 14, 951–960.
- Dingal P, Discher DE (2015). Systems mechano-biology: tension-inhibited protein turnover is sufficient to physically control gene circuits. *Biophys J* 108, 365A–366A.
- Diridollou S (2001). Mechanical properties of the skin under suction. *Skin Res Technol* 7, 127–127.
- Discher DE, Janmey P, Wang YL (2005). Tissue cells feel and respond to the stiffness of their substrate. *Science* 310, 1139–1143.
- Engler AJ, Sen S, Sweeney HL, Discher DE (2006). Matrix elasticity directs stem cell lineage specification. *Cell* 126, 677–689.
- Eroglu A, Hruszkewycz DP, dela Sena C, Narayanasamy S, Riedl KM, Kopec RE, Schwartz SJ, Curley RW Jr, Harrison EH (2012). Naturally occurring eccentric cleavage products of provitamin A beta-carotene function as antagonists of retinoic acid receptors. *J Biol Chem* 287, 15886–15895.
- Friedrichs J, Taubenberger A, Franz CM, Muller DJ (2007). Cellular remodeling of individual collagen fibrils visualized by time-lapse AFM. *J Mol Biol* 372, 594–607.
- Fuchs E, Tumber T, Guasch G (2004). Socializing with the neighbors: stem cells and their niche. *Cell* 116, 769–778.
- Gao Y, Li YF, Guo X, Wu ZG, Zhang W (2012). Loss of STAT1 in bone marrow-derived cells accelerates skeletal muscle regeneration. *PLoS One* 7, 9.
- Geiger B, Spatz JP, Bershadsky AD (2009). Environmental sensing through focal adhesions. *Nat Rev Mol Cell Biol* 10, 21–33.
- Goldman RD, Shumaker DK, Erdos MR, Eriksson M, Goldman AE, Gordon LB, Gruenbaum Y, Khuon S, Mendez M, Varga R, Collins FS (2004). Accumulation of mutant lamin A causes progressive changes in nuclear architecture in Hutchinson-Gilford progeria syndrome. *Proc Natl Acad Sci USA* 101, 8963–8968.
- Gudas LJ (2013). Retinoids induce stem cell differentiation via epigenetic changes. *Semin Cell Dev Biol* 24, 701–705.
- Guilak F, Alexopoulos LG, Haider MA, Ting-Beall HP, Setton LA (2005). Zonal uniformity in mechanical properties of the chondrocyte pericellular matrix: micropipette aspiration of canine chondrons isolated by cartilage homogenization. *Ann Biomed Eng* 33, 1312–1318.
- Harada T, Swift J, Irianto J, Shin JW, Spinler KR, Athirasala A, Diegmiller R, Dingal P, Ivanovska IL, Discher DE (2014). Nuclear lamin stiffness is a barrier to 3D migration, but softness can limit survival. *J Cell Biol* 204, 669–682.
- Hayashi C, Hasegawa U, Saita Y, Hemmi H, Hayata T, Nakashima K, Ezura Y, Amagasa T, Akiyoshi K, Noda M (2009). Osteoblastic bone formation is induced by using nanogel-crosslinking hydrogel as novel scaffold for bone growth factor. *J Cell Physiol* 220, 1–7.
- Heath DJ, Downes S, Verderio E, Griffin M (2001). Characterization of tissue transglutaminase in human osteoblast-like cells. *J Bone Miner Res* 16, 1477–1485.
- Ho CY, Jaalouk DE, Vartiainen MK, Lammerding J (2013). Lamin A/C and emerin regulate MKL1-SRF activity by modulating actin dynamics. *Nature* 497, 507–511.
- Jain N, Iyer KV, Kumar A, Shivashankar GV (2013). Cell geometric constraints induce modular gene-expression patterns via redistribution of HDAC3 regulated by actomyosin contractility. *Proc Natl Acad Sci USA* 110, 11349–11354.
- Kaartinen MT, El-Maadawy S, Rasanen NH, McKee MD (2002). Tissue transglutaminase and its substrates in bone. *J Bone Miner Res* 17, 2161–2173.
- Katz EP, Li S (1973). Structure and function of bone collagen fibrils. *J Mol Biol* 80, 1–5.
- Kramann R, Schneider RK, DiRocco DP, Machado F, Fleig S, Bondzie PA, Henderson JM, Ebert BL, Humphreys BD (2015). Perivascular Gli1(+) progenitors are key contributors to injury-induced organ fibrosis. *Cell Stem Cell* 16, 51–66.
- Kubben N, Voncken JW, Konings G, van Weeghel M, van den Hoogenhof MMG, Gijbels M, van Erk A, Schoonderwoerd K, van den Bosch B, Dahlmans V, et al. (2011). Post-natal myogenic and adipogenic developmental Defects and metabolic impairment upon loss of A-type lamins. *Nucleus* 2, 195–207.
- Liu HJ, Wen J, Xiao Y, Liu J, Hopyan S, Radisic M, Simmons CA, Sun Y (2014). In situ mechanical characterization of the cell nucleus by atomic force microscopy. *ACS Nano* 8, 3821–3828.
- Lovett DB, Shekhar N, Nickerson JA, Roux KJ, Lele TP (2013). Modulation of nuclear shape by substrate rigidity. *Cell Mol Bioeng* 6, 230–238.
- Majkut S, Idema T, Swift J, Krieger C, Liu A, Discher DE (2013). Heart-specific stiffening in early embryos parallels mixer and myosin expression to optimize beating. *Curr Biol* 23, 2434–2439.
- Maruhashi T, Kii I, Saito M, Kudo A (2010). Interaction between periostin and BMP-1 promotes proteolytic activation of lysyl oxidase. *J Biol Chem* 285, 13294–13303.
- McClintock D, Ratner D, Lokuge M, Owens DM, Gordon LB, Collins FS, Djabali K (2007). The mutant form of lamin A that causes Hutchinson-Gilford progeria is a biomarker of cellular aging in human skin. *PLoS One* 2, e1269.
- Medyouf H, Mossner M, Jann JC, Nolte F, Raffel S, Herrmann C, Lier A, Eisen C, Nowak V, Zens B, et al. (2014). Myelodysplastic cells in patients reprogram mesenchymal stromal cells to establish a transplantable stem cell niche disease unit. *Cell Stem Cell* 14, 824–837.
- MEEK KM, Chapman JA, Hardcastle RA (1979). Staining pattern of collagen fibrils - improved correlation with sequence data. *J Biol Chem* 254, 710–714.
- Miyaishi O, Kozaki K, Iida K, Isobe K, Hashizume Y, Saga S (1998). Elevated expression of PDI family proteins during differentiation of mouse F9 teratocarcinoma cells. *J Cell Biochem* 68, 436–445.
- Mukherjee S, Date A, Patravale V, Korting HC, Roeder A, Weindl G (2006). Retinoids in the treatment of skin aging: an overview of clinical efficacy and safety. *Clin Interv Aging* 1, 327–348.
- Musah S, Wrighton PJ, Zaltsman Y, Zhong X, Zorn S, Parlato MB, Hsiao C, Palecek SP, Chang Q, Murphy WL, Kiessling LL (2014). Substratum-induced differentiation of human pluripotent stem cells reveals the

- coactivator YAP is a potent regulator of neuronal specification. *Proc Natl Acad Sci USA* 111, 13805–13810.
- Nassar D, Latil M, Boeckx B, Lambrechts D, Blanpain C (2015). Genomic landscape of carcinogen-induced and genetically induced mouse skin squamous cell carcinoma. *Nat Med* 21, 946–954.
- Nelson CM, Bissell MJ (2006). Of extracellular matrix, scaffolds, signaling: tissue architecture regulates development, homeostasis, cancer. *Annu Rev Cell Dev Biol* 22, 287–309.
- Neuman RE, Logan MA (1950). The determination of collagen and elastin in tissues. *J Biol Chem* 186, 549–556.
- Okumura K, Hosoe Y, Nakajima N (2004). c-Jun and Sp1 family are critical for retinoic acid induction of the lamin A/C retinoic acid-responsive element. *Biochem Biophys Res Commun* 320, 487–492.
- Olive M, Harten I, Mitchell R, Beers JK, Djabali K, Cao K, Erdos MR, Blair C, Funke B, Smoot L, et al. (2010). Cardiovascular pathology in hutchinson-gilford progeria: correlation with the vascular pathology of aging. *Arterioscler Thromb Vasc Biol* 30, 2301–U2636.
- Pagliara S, Franze K, McClain CR, Wylde GW, Fisher CL, Franklin RJM, Kabla AJ, Keyser UF, Chalut KJ (2014). Auxetic nuclei in embryonic stem cells exiting pluripotency. *Nat Mater* 13, 638–644.
- Park D, Spencer JA, Koh BI, Kobayashi T, Fujisaki J, Clemens TL, Lin CP, Kronenberg HM, Scadden DT (2012). Endogenous bone marrow MSCs are dynamic, fate-restricted participants in bone maintenance and regeneration. *Cell Stem Cell* 10, 259–272.
- Pelham RJ, Wang YL (1997). Cell locomotion and focal adhesions are regulated by substrate flexibility. *Proc Natl Acad Sci USA* 94, 13661–13665.
- Pittenger MF, Mackay AM, Beck SC, Jaiswal RK, Douglas R, Mosca JD, Moorman MA, Simonetti DW, Craig S, Marshak DR (1999). Multilineage potential of adult human mesenchymal stem cells. *Science* 284, 143–147.
- Raab M, Swift J, Dingal P, Shah P, Shin JW, Discher DE (2012). Crawling from soft to stiff matrix polarizes the cytoskeleton and phosphoregulates myosin-II heavy chain. *J Cell Biol* 199, 669–683.
- Rehfeldt F, Brown AEX, Raab M, Cai SS, Zajac AL, Zemel A, Discher DE (2012). Hyaluronic acid matrices show matrix stiffness in 2D and 3D dictates cytoskeletal order and myosin-II phosphorylation within stem cells. *Integr Biol* 4, 422–430.
- Roosa SMM, Liu YL, Turner CH (2011). Gene expression patterns in bone following mechanical loading. *J Bone Miner Res* 26, 100–112.
- Schellenberg A, Jousen S, Moser K, Hampe N, Hersch N, Hemeda H, Schnitker J, Denecke B, Lin Q, Pallua N, et al. (2014). Matrix elasticity, replicative senescence and DNA methylation patterns of mesenchymal stem cells. *Biomaterials* 35, 6351–6358.
- Shimono K, Tung WE, Macolino C, Chi AHT, Didizian JH, Mundy C, Chandraratna RA, Mishina Y, Enomoto-Iwamoto M, Pacifici M, Iwamoto M (2012). Potent inhibition of heterotopic ossification by nuclear retinoic acid receptor-gamma agonists. *Nat Med* 18, 1592.
- Silverman BW (1981). Using kernel density estimates to investigate multimodality. *J R Stat Soc Ser A* 43, 97–99.
- Sodek J, McKee MD (2000). Molecular and cellular biology of alveolar bone. *Periodontology* 24, 99–126.
- Solon J, Levental I, Sengupta K, Georges PC, Janmey PA (2007). Fibroblast adaptation and stiffness matching to soft elastic substrates. *Biophys J* 93, 4453–4461.
- Staunton JR, Doss BL, Lindsay S, Ros R (2016). Correlating confocal microscopy and atomic force indentation reveals metastatic cancer cells stiffen during invasion into collagen I matrices. *Sci Rep* 6, 19686.
- Stein GS, Lian JB, Owen TA (1990). Relationship of cell-growth to the regulation of tissue-specific gene-expression during osteoblast differentiation. *FASEB J* 4, 3111–3123.
- Stolz M, Gottardi R, Raiteri R, Miot S, Martin I, Imer R, Stauffer U, Raducanu A, Duggelin M, Baschong W, et al. (2009). Early detection of aging cartilage and osteoarthritis in mice and patient samples using atomic force microscopy. *Nat Nanotechnol* 4, 186–192.
- Swift J, Harada T, Buxboim A, Shin J-W, Tang H-Y, Speicher DW, Discher DE (2013a). Label-free mass spectrometry exploits dozens of detected peptides to quantify lamins in wildtype and knockdown cells. *Nucleus* 4, 450–459.
- Swift J, Ivanovska IL, Buxboim A, Harada T, Dingal PCDP, Pinter J, Pajewski JD, Spinler KR, Shin J-W, Tewari M, et al. (2013b). Nuclear lamin-A scales with tissue stiffness and enhances matrix-directed differentiation. *Science* 341, 1240104.
- Tajima K, Takaishi H, Takito J, Tohmonda T, Yoda M, Ota N, Kosaki N, Matsumoto M, Ikegami H, Nakamura T, et al. (2010). Inhibition of STAT1 accelerates bone fracture healing. *J Orthop Res* 28, 937–941.
- Talwar S, Jain N, Shivashankar GV (2014). The regulation of gene expression during onset of differentiation by nuclear mechanical heterogeneity. *Biomaterials* 35, 2411–2419.
- Talwar S, Kumar A, Rao M, Menon GI, Shivashankar GV (2013). Correlated spatio-temporal fluctuations in chromatin compaction states characterize stem cells. *Biophys J* 104, 553–564.
- Termine JD, Kleinman HK, Whitson SW, Conn KM, McGarvey ML, Martin GR (1981). Osteonectin, a bone-specific protein linking mineral to collagen. *Cell* 26, 99–105.
- Titushkin I, Cho M (2007). Modulation of cellular mechanics during osteogenic differentiation of human mesenchymal stem cells. *Biophys J* 93, 3693–3702.
- Wang Y, Chen JX, Lee CSD, Nizkorodov A, Riemenschneider K, Martin D, Hyzy S, Schwartz Z, Boyan BD (2010). Disruption of Pdia3 gene results in bone abnormality and affects 1 alpha,25-dihydroxy-vitamin D-3-induced rapid activation of PKC. *J Steroid Biochem Mol Biol* 121, 257–260.
- Watt FM, Huck WTS (2013). Role of the extracellular matrix in regulating stem cell fate. *Nat Rev Mol Cell Biol* 14, 467–473.
- Williams JA, Kondo N, Okabe T, Takeshita N, Pilchak DM, Koyama E, Ochiai T, Jensen D, Chu ML, Kane MA, et al. (2009). Retinoic acid receptors are required for skeletal growth, matrix homeostasis and growth plate function in postnatal mouse. *Dev Biol* 328, 315–327.
- Wipff PJ, Rifkin DB, Meister JJ, Hinz B (2007). Myofibroblast contraction activates latent TGF-beta 1 from the extracellular matrix. *J Cell Biol* 179, 1311–1323.
- Xiao LP, Naganawa T, Obugunde E, Gronowicz G, Ornitz DM, Coffin JD, Hurlley MM (2004). Stat1 controls postnatal bone formation by regulating fibroblast growth factor signaling in osteoblasts. *J Biol Chem* 279, 27743–27752.
- Yener B, Acar E, Aguis P, Bennett K, Vandenberg SL, Plopper GE (2008). Multiway modeling and analysis in stem cell systems biology. *BMC Syst Biol* 2, 63.
- Yim EKF, Darling EM, Kulangara K, Guilak F, Leong KW (2010). Nanotopography-induced changes in focal adhesions, cytoskeletal organization, mechanical properties of human mesenchymal stem cells. *Biomaterials* 31, 1299–1306.
- Yourek G, Hussain MA, Mao JJ (2007). Cytoskeletal changes of mesenchymal stem cells during differentiation. *ASAIO J* 53, 219–228.
- Zemel A, Rehfeldt F, Brown AEX, Discher DE, Safran SA (2010). Optimal matrix rigidity for stress-fibre polarization in stem cells. *Nat Phys* 6, 468–473.
- Zhang JQ, Lian QZ, Zhu GL, Zhou F, Sui L, Tan C, Mutalif RA, Navasankari R, Zhang YL, Tse HF, Stewart CL, Colman A (2011). A human iPSC model of Hutchinson Gilford progeria reveals vascular smooth muscle and mesenchymal stem cell defects. *Cell Stem Cell* 8, 31–45.

Supplemental Materials

Molecular Biology of the Cell

Ivanovska et al.

Cross-linked matrix rigidity and soluble retinoids synergize in nuclear lamina regulation of stem cell differentiation

Irena L. Ivanovska et al.

Supplemental materials

Supplemental materials and methods

Supplemental figures S1 – S7

Supplemental references

Supplemental materials and methods

Cell Culture Human-derived alveolar epithelial (A549, CCL-185) cells were cultured according to protocols provided by the supplier (American Type Culture Collection). Primary human mesenchymal stem cells (anonymous donors with Institutional Review Board approvals) were obtained from the Xenograft Core Facility at the University of Pennsylvania School of Medicine. They were cultured in low glucose Dulbecco's modification of Eagle's medium (DMEM, Invitrogen) with 10% fetal bovine serum (FBS, Sigma Aldrich).

Mesenchymal differentiation of iPSCs without EB formation. iPSC lines were derived from primary fibroblasts and were obtained from 'The Progeria Research Foundation Cell & Tissue Bank', Univ. Ottawa. Derivation of iPSC-MSCs is done as described in (Zou *et al.*, 2013), briefly three days after splitting, iPS medium was replaced with MSC medium, which consisted of low glucose Dulbecco's modification of Eagle's medium (DMEM, Invitrogen) with 10% fetal bovine serum (FBS, Sigma Aldrich) and 1% penicillin/streptomycin. The MSC medium was changed every 2 days. After 14 days culture, the cells were trypsinized (0.25% trypsin/1 mM EDTA, Difco-Sigma) and expanded in MSC medium on 0.1% gelatin coated dishes (Becton Dickinson). When confluent (3–5 days), cells were harvested with 0.025% trypsin-EDTA and then regularly passaged at a 1:3 ratio. Usually, after the third trypsinization, a morphologically homogeneous population of fibroblast-like cells became evident and was used in the analysis of MSC phenotypic characteristics and differentiation potential.

Lamin knockdown. Cells were passaged to 70% confluency 24 hr before transfection.

A complex of siRNA (30 nM; siLMNA1, 5'-GGUGGUGACGAUCUGGGCU-3' or siLMNA2, 5'- AACUGGACUCCAGAAGAACAUC-3') was transfected into cells with Lipofectamine 2000 reagent (1 µg/mL) as described in the manufacturer's protocol (Invitrogen).

Drug treatment protocol. Cultured cells were treated with control solvent (0.15% EtOH, 0.15% DMSO in media with 10% FBS), or solvent containing: all-trans RA (1 µM, Fisher Scientific); adapalene; CD437 (0.1 µM, Tocris Bioscience); CD1530; CD2665 (1 µM, Tocris Bioscience); AGN-193109 (1 µM, Santa Cruz Biotechnology).

Preparation of stiff substrates. Polyacrylamide hydrogels of 0.3 kPa to 40 kPa stiffness were prepared as described previously (Buxboim *et al.*, 2010). Gels for cell culture were further coated with type-I rat tail collagen or freshly prepared human fibronectin (BD Biosciences) as follows: Sulfo-Sanpah (Fisher Scientific) was dissolved in 50 mM, pH 8 HEPES to a concentration of 0.5 mg/mL and pipetted to form a complete coverage of the gels. Gels were placed inside a UV chamber and illuminated for 10 min by 365 nm illumination. To minimize collagen fiber formation, collagen was first mixed in equal volume of 4 °C 0.1 M acetic acid (Fisher Scientific) and then diluted in 4 °C 50 mM, pH 8 HEPES to a final concentration of 0.2 mg/mL. Protein was incubated on the gels while on a shaker overnight at 37 °C. Prior to seeding cells, gels were UV-sterilized in cell culture hood for two hours. Gels were kept hydrated in PBS or deionized water during all preparation steps.

Immunofluorescence imaging. Cells were rinsed with PBS, fixed with 4% paraformaldehyde (Fisher) for 20 min, washed twice with PBS and permeabilized with 0.5% Triton-X (Fisher) in PBS for 20 min. Cells were then treated with 5% BSA (blocking solution) for 1 hr. Following two additional PBS washes, samples were incubated overnight with primary antibodies at 1:300 dilution in 2% BSA solution with gentle agitation at 4 °C. The primary antibodies used were: lamin-A/C mouse monoclonal sc-7292; lamin-B goat polyclonal sc-6217; RAR-gamma rabbit polyclonal PA5-21463 (Thermo Scientific). Cells were washed twice in PBS and incubated with the corresponding secondary antibodies at 1:500 dilution for 45 minutes (Alexa Fluor 546, 594 and 647 nm; Invitrogen). Adherent cells on gels or glass coverslips were mounted with mounting media (Invitrogen ProLong Gold Antifade Reagent) or sometimes imaged with fixation and no mounting. Images of adherent cells were taken with an Olympus IX71 microscope in epifluorescence or else a confocal laser scanning mode with the 488 nm and 543 nm laser lines, for GFP and Alexa 546 dyes, respectively. All images for quantitative analysis in a given experiment were taken under the same imaging conditions.

mRNA profiling of tissues and cells. Human and mouse tissue transcript data (1.0 ST datasets) was downloaded from: http://www.affymetrix.com/support/technical/sample_data/exon_array_data.affx.

Transcriptomes from whole genome microarrays (Affymetrix, Santa Clara, CA) were for mouse adult tissues: brain, heart, kidney, liver, lung, ovary, muscle, spleen, testis and thymus ($n = 3$); and human adult tissues: brain, breast, heart, kidney, liver, pancreas, prostate, muscle, spleen, testis and thyroid ($n = 3$). Pearson correlations between *Col1a1* and a range of genes were calculated from these data sets using Mathematica (Wolfram) (Figs. 2 B, C).

mRNA levels were profiled in MSCs subjected to lamin-A,C knockdown ($n = 3$) (Fig. S6B). Total RNA was extracted from cells using Trizol and isolated by RNeasy (Qiagen) according to manufacturer's protocol. Total RNA was amplified and converted to cDNA using WT-Ovation Pico kit (NuGen) and converted to ST-cDNA, fragmented and biotin-functionalized using WT-Ovation Exon Module (NuGen). Hybridization cocktails were prepared at 45.4, 15.1 and 7.6 ng/ μ L ST-cDNA and mixed with Eukaryotic Hybridization Controls (GeneChip) at proportional concentrations. Each Sample was interrogated by sequential hybridization, rinse and scan cycles on a single Human Gene 1.0 ST DNA microarray (Affymetrix, Santa Clara, CA), from low to high concentration, and followed by two rinse-scan cycles in which no sample was added. In each experiment the scanned intensities that were obtained from all samples, five scans per array, were mutually RMA-summarized to transcription clusters gene levels so that the average and standard deviation could be calculated for each gene.

Quantitative mass spectrometry (MS). We have previously described methods for preparing primary tissue samples for MS (Swift *et al.*, 2013b) and for quantifying species-specific peptides (Swift *et al.*, 2013a). Briefly, tissue samples were flash-frozen in liquid nitrogen and finely ground between metal plates on dry ice. Proteins were then solubilized in 1x NuPAGE LDS buffer (with protease inhibitor cocktail and 0.1% β -mercaptoethanol) using sonication and heating (80 °C, 10 mins). Insoluble material was separated by centrifugation. SDS-PAGE gels (NuPAGE 4-12% Bis-Tris, Invitrogen) were loaded with 2 – 14 μ L of lysate per lane (load volumes were adjusted to avoid overloading and smearing, diluting the lysates with additional 1x NuPAGE LDS buffer as necessary). Gel electrophoresis was run for 10 min at 100 V and 15 min at 160 V. Excised gel sections were washed (50% 0.2 M ammonium bicarbonate (AB) solution, 50% acetonitrile (ACN), 30 min at 37 °C), dried by lyophilization, incubated with a reducing agent (20 mM tris(2-carboxyethyl)phosphine (TCEP) in 25 mM AB solution at pH 8.0, 15 min at 37 °C) and alkylated (40 mM

iodoacetamide (IAM) in 25 mM AB solution at pH 8.0, 30 min at 37 °C). The gel sections were dried by lyophilization before in-gel trypsinization (20 µg/mL sequencing grade modified trypsin in buffer as described in the manufacturer's protocol (Promega), 18 hr at 37 °C with gentle shaking). The resulting solutions of tryptic peptides were acidified by addition of 50% digest dilution buffer (60 mM AM solution with 3% formic acid).

Peptide separations (5 µL injection volume) were performed on 15-cm PicoFrit column (75 µm inner diameter, New Objective) packed with Magic 5 µm C18 reversed-phase resin (Michrom Bioresources) using a nanoflow high-pressure liquid chromatography system (Eksigent Technologies), which was coupled online to a hybrid LTQ-Orbitrap XL mass spectrometer (Thermo Fisher Scientific) via a nanoelectrospray ion source. Chromatography was performed with Solvent A (Milli-Q water with 0.1% formic acid) and Solvent B (acetonitrile with 0.1% formic acid). Peptides were eluted at 200 nL/min for 3–28% B over 42 min, 28–50% B over 26 min, 50–80% B over 5 min, 80% B for 4.5 min before returning to 3% B over 0.5 min. To minimize sample carryover, a fast blank gradient was run between each sample. The LTQ-Orbitrap XL was operated in the data-dependent mode to automatically switch between full scan MS ($m/z = 350$ –2000 in the orbitrap analyzer (with resolution of 60,000 at m/z 400) and the fragmentation of the six most intense ions by collision-induced dissociation in the ion trap mass analyzer.

Raw mass spectroscopy data was processed using Elucidator (version 3.3, Rosetta Biosoftware). Peptide and protein annotations were made using SEQUEST (version 28, Thermo Fisher Scientific) with full tryptic digestion and up to 2 missed cleavage sites. Peptide masses were selected between 800 and 4500 amu with peptide mass tolerance of 1.1 amu and fragment ion mass tolerance of 1.0 amu. Peptides were searched against databases compiled from UniRef100 mouse and human, plus contaminants and a reverse decoy database. The peptide database was modified to search for alkylated cysteine residues (monoisotopic mass change, $\Delta = +57.021$ Da) and oxidized methionine ($\Delta = +15.995$ Da). In proteomic profiling experiments, we also considered the acetylation of lysine ($\Delta = +42.011$ Da), methylation of lysine and arginine ($\Delta = +14.016$ Da) and phosphorylation of serine, tyrosine, threonine, histidine and aspartate ($\Delta = +79.966$ Da). Ion currents of modified peptides were summed with their parent peptide. Peptides derived from trypsin or keratin were considered to be contaminants and were not used in subsequent calculations.

Micropipette aspiration. Micropipette aspiration was performed as described previously (Pajerowski *et al.*, 2007), (Swift *et al.*, 2013b). For nucleus aspiration cells were treated with 0.2 $\mu\text{g/ml}$ Latrunculin A (Sigma) for 1 hour at 37°C, detached with trypsin/EDTA, centrifuged and resuspended in aspiration buffer of 135 mM NaCl, 5mM KCl, 5 mM HEPES, 1.8 mM CaCl₂, 2 mM MgCl₂, 2% BSA, 1:3000 propidium iodide (Molecular Probes). Nuclei were stained with Hoechst 33342 (Molecular Probes). Nuclei were aspirated under negative pressure inside a micropipette and the membrane extension was imaged with Nikon TE300 inverted microscope coupled with a digital CCD camera (Roper Scientific, Tuscan AZ), using a 60x oil immersion objective. Suction was applied by syringe and the corresponding pressure was measured by a pressure transducer (Validyne) calibrated by a mercury U-tube manometer. Image analysis was done using ImageJ. The compliance was calculated as described in (Pajerowski *et al.*, 2007) and stiffness is determined from (Majkut *et al.*, 2013). For grafts aspiration a micropipette with diameter of 15 μm is used to deform a freshly excised piece of tissue. After aspiration, the graft was divided in two pieces and one was treated with transglutaminase (Sigma-Aldrich T5398, concentration 100 $\mu\text{g/mL}$ in of 50 mM TRIS buffer, 5 mM CaCl₂, 2 mM dithiothreitol at pH 7.4) for 30 minutes at 37⁰ C and 5% CO₂ and aspirated again and the other one was treated without transglutaminase and it was used as a control.

MSC xenografts in mouse. All animal experiments were planned and performed according to IACUC protocols. Fresh human bone marrow mesenchymal stem cells were isolated from bone marrow (anonymous donors with Institutional Review Board approvals) from the Xenograft Core Facility at the University of Pennsylvania School of Medicine. MSC were cultured and expanded cultured in low glucose Dulbecco's modification of Eagle's medium (DMEM, Invitrogen) with 10% fetal bovine serum (FBS, Sigma Aldrich) and are used at low passage ($P < 5$). 2×10^6 cells were mixed with Matrigel (#356234, BD Biosciences) according to the manufacturer protocol and injected subcutaneously in mice flank. Cells were either not treated or pretreated with osteogenic media and RA antagonist CD 2665 (1 μM , Tocris Bioscience) for 3 days. Mouse grafts that were isolated after 4weeks growth were also mixed with DiR (Life Technologies) labeled beads prior to injection to insure the proper identification of the human cells localization upon extraction. Grafts that were left to grow for 12 weeks were not mixed with fluorescent

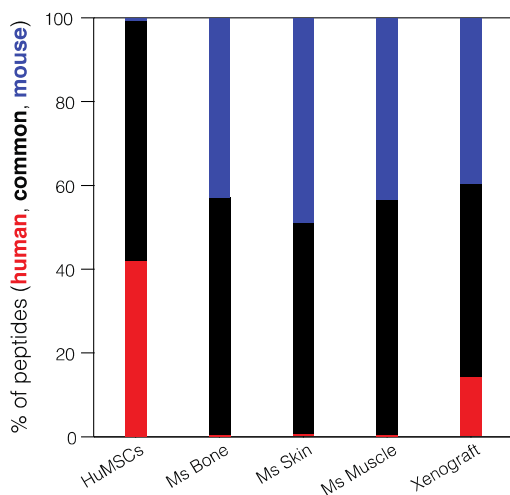
beads, their location was identified by imaging mouse injected with OsteoSense 750EX Fluorescent Imaging Agent (PerkinElmer) 24 hours earlier. After harvesting graft tissues and tissues from skin and bone, each tissue were cut into 3 pieces. One set of tissues were snap-frozen with liquid nitrogen for MS evaluation and the second and third set were fixed with PFA and stained for Alkaline Phosphatase Activity (ALP) and Alizarin red.

ALP and Alizarin Red staining. ALP staining of cells or tissues is performed immediately after their fixation in PFA. After washing with 10mM Tris buffer pH 7.2 samples were immersed in alkaline-dye solution of Fast Blue RR Salt (Sigma FBS-25) capsules dissolved in DW at concentration as it is indicated by the manufacturer and Naphthol AS-MX phosphatase solution. For Alizarin red staining, samples were washed with DW and immersed for 5 to 10 min in 1% Alizarin Red S (LC 106007) pH 4-4.3. After washing with DW the samples are imaged with color camera in bright field. The ALP or Alizarin Red is quantified from the blue or the red component respectively of the color images after deconvolution with Image J. The scale of the single color intensity (0-255) is inverted and normalized by the number of the pixels of the image.

Supplemental Figures

Figure S1.

A Count of peptides that are common or unique to mouse or human in cell, tissue and xenograft samples



B Collagen-I protein and transcript quantified across a range of tissues

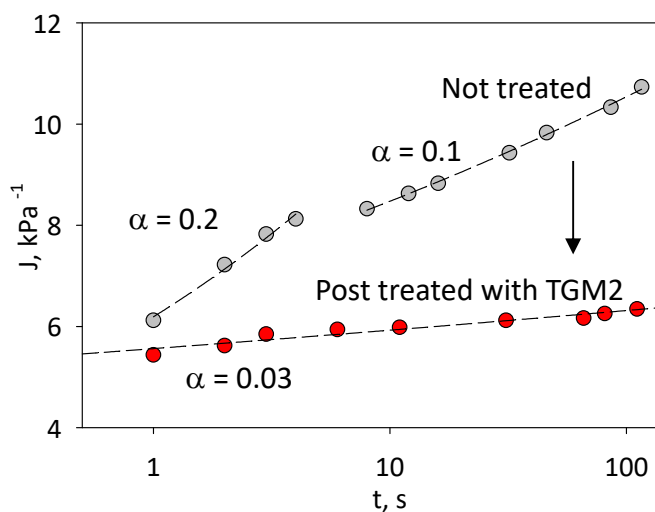
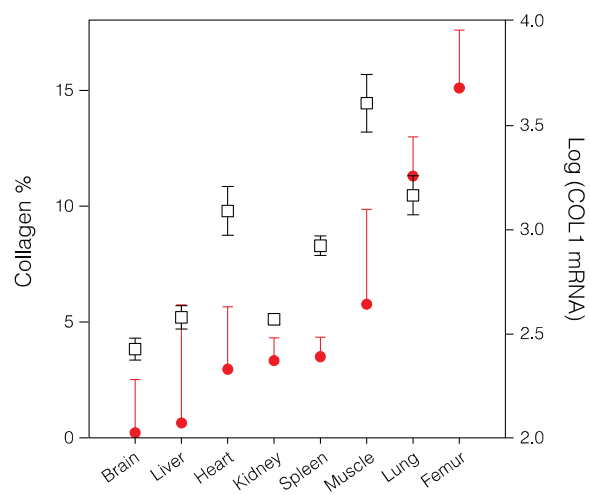
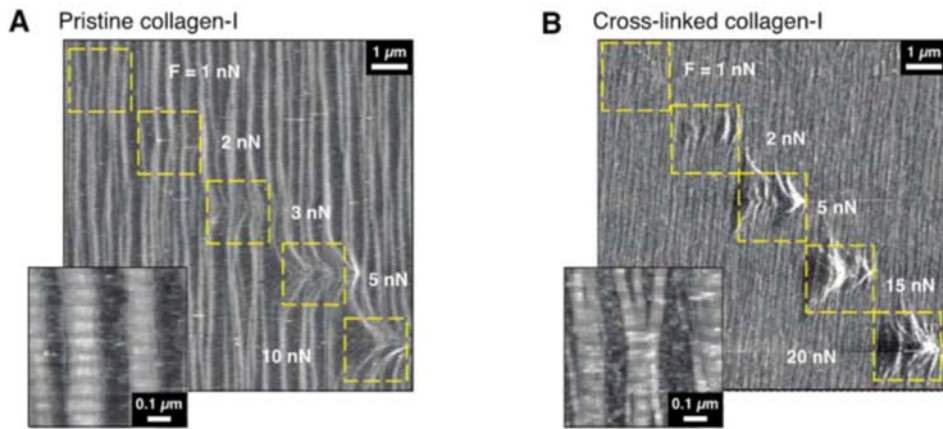


Fig. S1. (A) Human MSCs, primary mouse tissues (bone skin and muscle) and a xenograft (human MSCs in mouse flank, 4 weeks growth) were profiled by mass spectrometry proteomics. By comparison to databases (SEQUEST and NCBI BLAST), peptides were classified as being unique to mouse, human or common to both species. Samples from singular sources had ~ 44% uniquely native peptides and a low

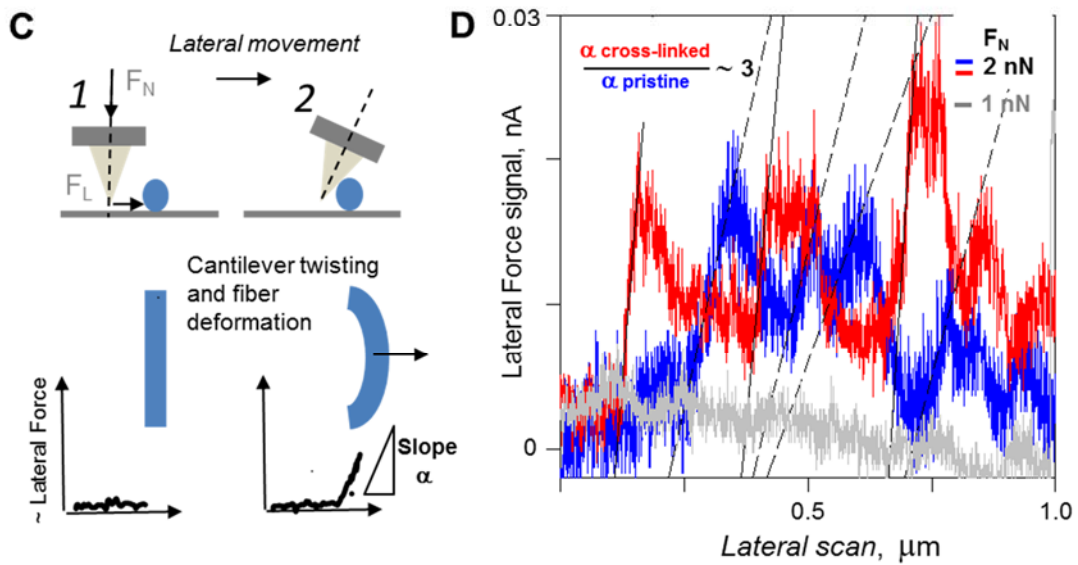
false positive rate of identifying foreign material ($< 0.8\%$ when considering peptides from proteins detected with two-or-more peptides-per-protein). The xenograft sample contained a significant number of human peptides, confirming that material derived from the MSCs persisted in the tumor for at least 4 weeks. A protein level analysis of the samples is shown in Fig. 2A. (B) Earlier work has shown that collagen protein and transcript levels are higher in stiffer tissues (Neuman and Logan, 1950). (C) Compliance of the excised xenograft aspirated for 100 sec is calculated as described in with α being higher for more viscous materials (Pajeroski *et al.*, 2007). The power law fit shows that a 30 min treatment with transglutaminase (TGM2) makes the tissue less viscous and less compliant, consistent with being more solid-like and stiffer.

Figure S2.

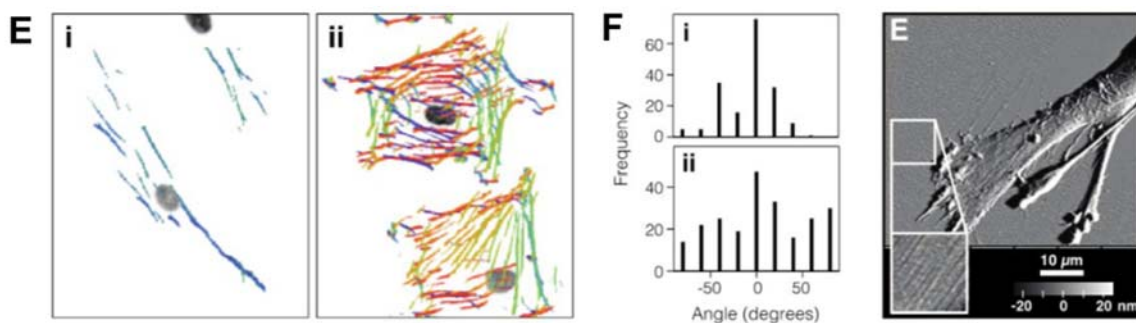
AFM scratching with increasing normal force shows robustness of cross-linked collagen-I film

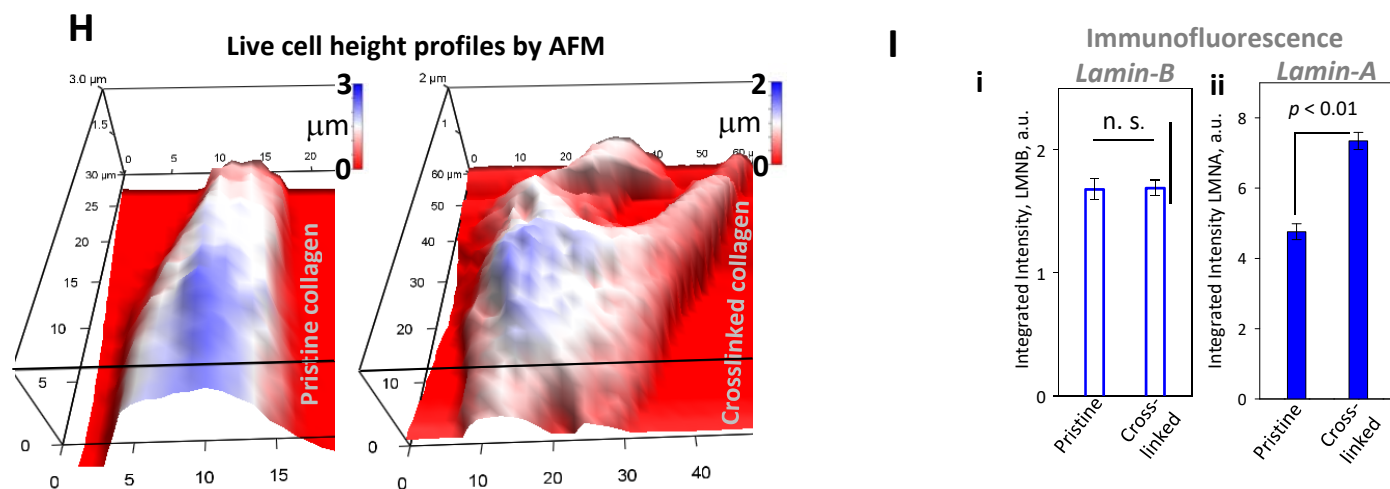


Fibril resistance to lateral forces torques the AFM tip



Orientation of stress fibers on pristine and cross-linked collagen-1 films



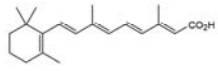
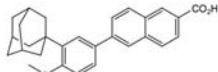
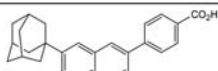
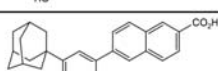
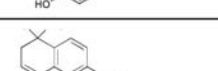
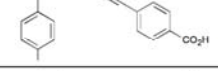


S2. Scratching the surface of (A) pristine and (B) cross-linked collagen-I films with the tip of an AFM demonstrates the increased robustness of the cross-linked film. Insets show high-resolution images of collagen fibrils. (C) Schematic representation of the lateral movement of the AFM tip and interaction with a fibril. (D) Lateral Force signal (not calibrated) versus scan distance for pristine and crosslinked collagen films. In gray is shown the signal for 1nN loading force. When the tip is dragged across the fibrils with 2 nN loading force the tip is tilted due to the resistance felt by the collagen fibril and the fibrils are deformed to a point after which the tip slips over the fibril. Force – distance slopes on the fibrils on crosslinked films are consistently higher than those of pristine films with ratio between the averaged slopes ~ 3 . (E) Orientation of stress fibers in cells on (i) pristine collagen-1 and (ii) cross-linked films determined by a segmentation algorithm with different colors representing different directions of the fibers (Zemel *et al.*, 2010). Stress fibers are tightly aligned with the collagen fibrils on pristine films, but are at broadly distributed orientations on the cross-linked films. (F) Angle distributions of stress fibers in MSCs cultured on (i) pristine or (ii) cross-linked collagen-I films, with angles measured with respect to the long axis of the ellipse fitted to each individual cell. (G) AFM topography image of an MSC cultured for 5 days on a cross-linked collagen-1 film. Inset highlights the fibrillar collagen. (H) AFM images made in Force Volume mode of life cells on pristine and cross-linked films. (I) Cells spread on gels with different stiffness for 24 h hours and co-stained for Lamin-A and Lamin-B, have constant total lamin-B whereas lamin-A is increased with $\sim 50\%$

matrix is actually a comparatively passive mechanical stimuli that changes slowly compared to the dynamic remodeling of cellular actomyosin. To better understand the dynamic internal adaptation in response to changes in substrate mechanics, we measured changes in the elastic response of the nuclear region, as measured by AFM, in MSCs on cross-linked collagen films over a period of 2 weeks. Elasticity maps of cells cultured on films for 48 hours gave a mean E of about 30 kPa and revealed a highly heterogeneous response within cells. After 2 more days in culture, the elasticity of the nuclear region dropped to 10 kPa, suggesting that cells undergo a relaxation of cortical tension after an initial stage of intensive cytoskeletal remodeling. The stiffness continued to decrease monotonically for a week following plating before rising again after two weeks, with a far more homogeneous response over the entire cell. The elastic response at this late culture point became more complicated due to the establishment of cell-cell contacts and cell-induced matrix remodeling. However, up to 1 week following initial plating, we were able to make measurements only on isolated cells and topographical AFM images revealed no deposition of matrix. Plot shows mean values of Young's moduli obtained from the elasticity maps at the nuclear region and averaged from ~ 60 curves per cell and from 4 - 7 individual cells per day.

Figure S4.**Agonists and antagonists to the RA pathway**

A

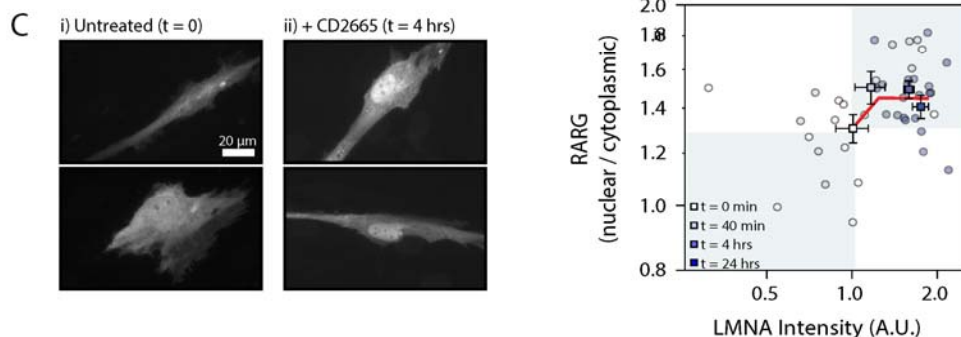
Compound	Description	Structure	Kd (nM)			Reference
			RAR α	RAR β	RAR γ	
All-trans retinoic acid ("RA")	Pan-RAR agonist		16 15 16 14	5 13 7 11	3 18 3 16	(Bernard, 1992) (Agarwal, 1996) (Szondy, 1997) (Gambone, 2002)
Adapalene	RAR β , γ agonist		1100	34	130	(Shroet, 1997)
CD1530	RAR γ agonist		2750	1500	150	(Bernard, 1992)
CD437	RAR γ agonist		6500	2480	77	(Bernard, 1992)
AGN193109 ("AGN")	Pan-RAR antagonist		22	8	7	(Gambone, 2002)
CD2665	RAR γ antagonist		> 1000	306	110	(Szondy, 1997)

Response in LMNA levels to RA pathway perturbations in MSCs

B

Sample identity	Passage number	Substrate	Time in culture	Method	Agonist	Antagonist	LMNA (Antagonist/Agonist)
MSC, 46 y.o. male	4	40 kPa gel	4 days	IF	RA	AGN	1.14
MSC, #1	3	glass	3 days	IF	CD1530	CD2665	1.17
MSC, 46 y.o. male	4	plastic	4 days	IF	RA	AGN	1.19
MSC, #1	3	cross-linked film	3 days	IF	CD1530	CD2665	1.39
MSC, 23 y.o. male	6	plastic	4 days	IF	CD1530	CD2665	1.39
MSC, 49 y.o. male	4	plastic	4 days	IF	RA	AGN	1.41
MSC, 30 y.o. female	6	plastic	6 days	Wb	RA	AGN	1.49
MSC, 30 y.o. female	6	plastic	8 days	MS	RA	AGN	1.71
MSC, 23 y.o. male	6	plastic	4 days	IF	RA	AGN	1.96
MSC, 23 y.o. male	5	plastic	4 days	IF	RA	AGN	2.04
MSC, 43 y.o. male; 46 y.o. female	5	plastic	36 hrs	Wb	RA	AGN	2.37
MSC, 43 y.o. male; 46 y.o. female	5	40 kPa gel	36 hrs	Wb	RA	AGN	2.76
MSC, 30 y.o. female	6	plastic	8 days	Wb	RA	AGN	3.63

AVG \pm SEM, 1.8 \pm 0.2

RARG construct's rapid kinetics with antagonist stimulation consistent with rapid increase in LMNA**Fig. S4.** (A) Table of properties of drugs that affect the RA pathway (Bernard *et al.*, 1992);(Agarwal *et al.*,

1996);(Szondy *et al.*, 1997);(Shroot and Michel, 1997);(Gambone *et al.*, 2002). (B) Table of MSC responses to agonists and antagonists to the RA pathway while cultured on stiff substrates, quantified by immunofluorescence (IF), western blot (Wb) and mass spectrometry (MS). The last column is averaged for each donor in Fig. 5B. (C) MSCs expressing the fluorescent RARG construct 'GEPRA' ("genetically encoded probe for RA" (Shimozono *et al.*, 2013)) cultured on plastic in the (i) absence and (ii) with the addition of RARG antagonist CD2665 for four hours. (iii) LMNA level, as determined by immunofluorescence, responded rapidly to the addition of CD2665, showing a 50% increase with an exponential half-life of ~ 2 hours. Consistent with Fig. 4Fiii, this process was concomitant with an increase in nuclear localization of transcription factor RARG.

Figure S5.

Response of LMNA levels to RA pathway perturbations in MSCs derived from iPS cells.

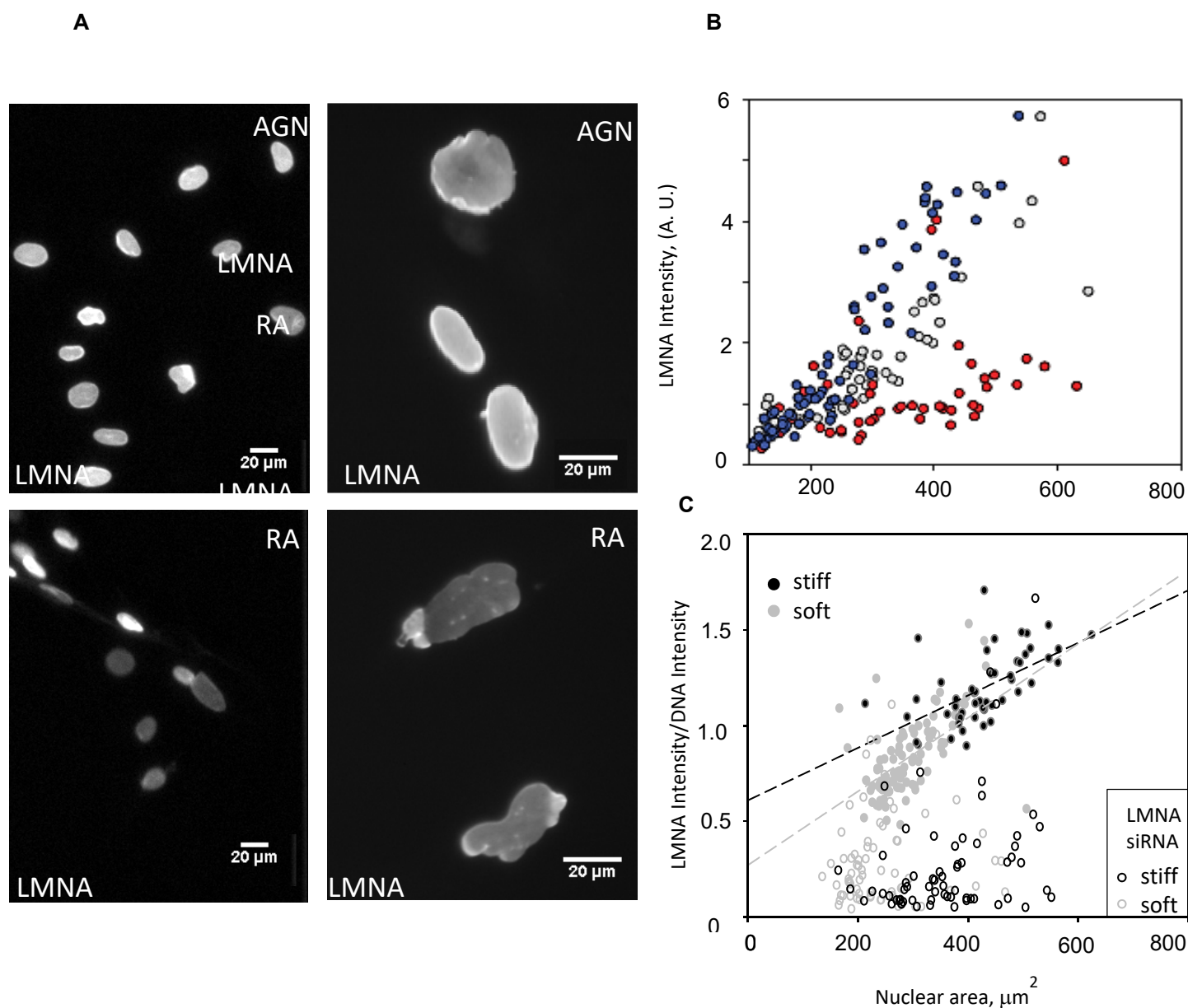
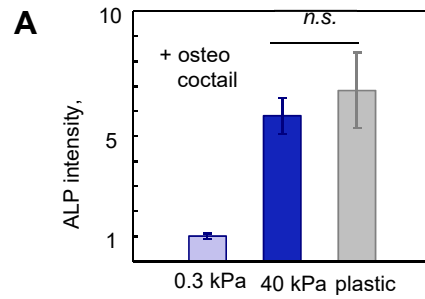


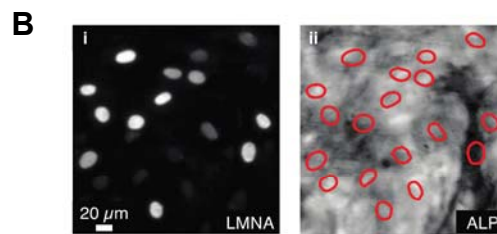
Fig. S5. (A) iPS cells differentiated to MSCs express LMNA as shown by immunofluorescent imaging, and the cells respond to AGN (upper images) and RA (lower images) treated for 4 days on plastic. (B) The corresponding LMNA quantification as determined by immunofluorescence, empty symbols – control, blue AGN, red RA. (C) IF of LMNA integrated intensity normalized with DNA integrated intensity (labeled with Hoescht) as a function of the nuclear area shows that data on soft and stiff substrate have similar slope and LMNA knockdown eliminates the nuclear spread area dependence.

Figure S6

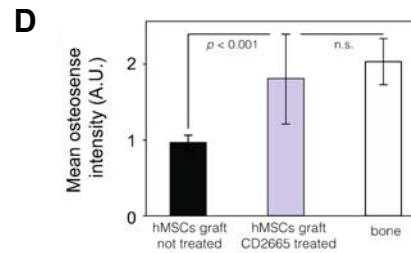
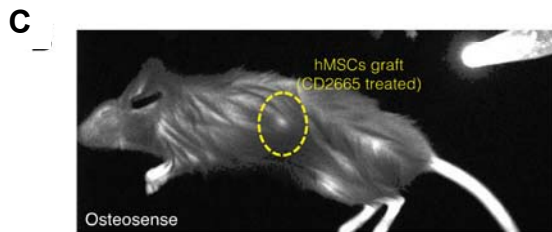
ALP staining in MSCs on gels and plastic *in vitro*



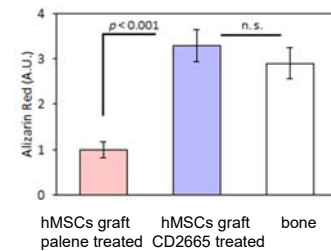
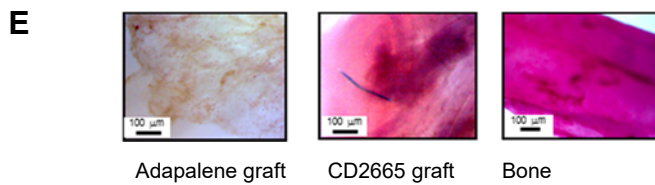
Cell-by-cell measurement of ALP staining in MSCs treated with RA antagonist *in vitro*



Osteosense imaging in live mice shows greater osteogenesis in xenograft tumors pretreated with RARG specific antagonist



Alizarin Red staining of Agonist (CD26650) and Antagonist (Adapalene) pretreated grafts



Antagonist increases *in vivo* osteogenesis: ALP staining

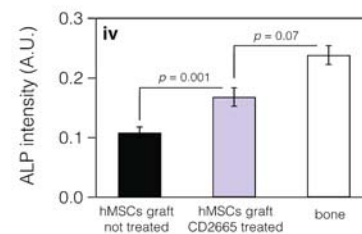
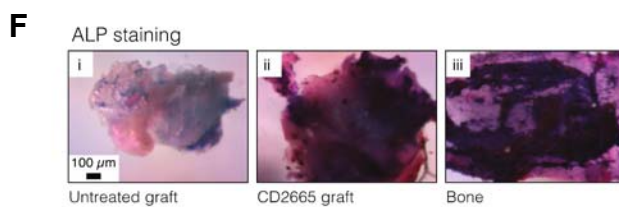


Fig. S6. (A) MSCs cultured on 40 kPa gel and plastic (rigid $E \sim$ GPa) in presence of osteo cocktail, show no significant difference in their osteogenic activity evaluated by the ALP signal and normalized to MSCs ALP signal on soft gel. (B) MSCs on rigid substrate were treated with a combination of osteo-induction media (OIM) and RARG-specific antagonist CD2665 (Fig. 5F). Osteogenic potential was estimated on a cell-by-cell basis and correlated with individual cellular levels of LMNA (i), by identifying and integrating ALP staining within the area of the nucleus (ii). (C) Further analysis of hMSCs grafted into mouse flank following pre-treatment with an RARG-specific antagonist is consistent with increased osteogenesis (see also Fig. 5G). Live mouse imaged after 12 weeks of MSCs graft growth with osteosense contrast agent (control tube in top right of image) used to show the location of a subcutaneous graft pre-treated with RAR-pathway antagonist CD2665. (D) Quantification of osteosense intensity suggests a significant increase in osteogenic character in grafts from MSCs pre-treated with CD2665. Error bars show standard deviation. (E) Alizarin red staining of hMSCs subcutaneous grafts pretreated with RARG-specific agonists Adapalene and antagonist CD2665 compared to bone shows that the antagonist enhanced osteogenesis and agonist suppressed osteogenesis *in vivo*. (F) In separate experiment excised tissues of MSCs antagonist pretreated graft was stained with ALP and compared to bone and untreated graft: (i) graft from untreated MSCs; (ii) graft from MSCs pre-treated for three days with CD2665; (iii) mouse bone, (iv) Quantification of ALP intensity.

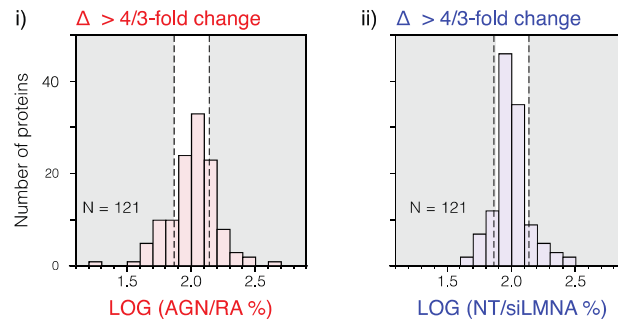
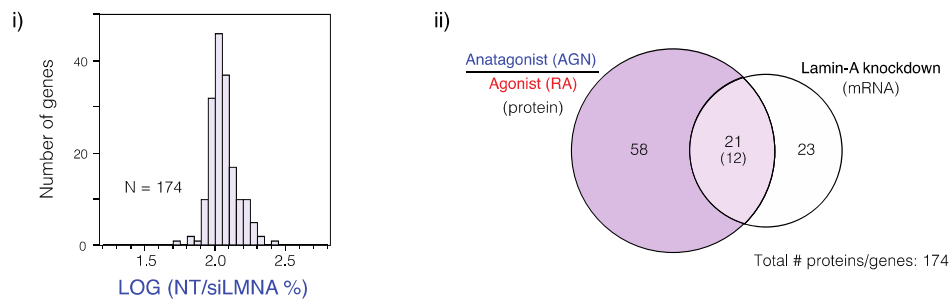
Figure S7.**A Changes to the proteome induced by perturbation to the RA-pathway or siLMNA****B Comparison of proteome changes during RA-treatment and mRNA changes with siLMNA**

Fig. S7. Proteomic profiling of MSCs subjected to lamin knockdown or perturbation to the retinoic acid (RA) pathway. (A) Histograms showing the width of distribution of protein level changes induced in MSCs by (i) RA-pathway antagonist AGN vs. agonist RA (ii) untreated vs. siLMNA. The levels of 121 proteins common to both samples were quantified by mass spectrometry (MS) with a minimum of 3 tryptic peptides detected per protein (see Figs. 6A, B). (B) Protein changes during RA-pathway perturbation were also compared to transcript changes during LMNA knockdown. (i) Histogram showing changes in levels of 174 mRNA transcripts, quantified by microarray, that were also quantified by MS. (ii) Venn diagram showing the proteins and transcripts that varied by more than 4/3-fold. 21 genes/proteins changed in both experiments, and of these, 12 showed correlated changes. The genes/proteins common to this overlap set and that shown in Fig. 6B are: ALCAM, STAT1, LMNA, EHD2, MVP and P4HA2.

Supplemental references

Agarwal, C., Chandraratna, R.A.S., Johnson, A.T., Rorke, E.A., and Eckert, R.L. (1996). AGN193109 is a highly effective antagonist of retinoid action in human ectocervical epithelial cells. *Journal of Biological Chemistry* **271**, 12209-12212.

Bernard, B.A., Bernardon, J.M., Delescluse, C., Martin, B., Lenoir, M.C., Maignan, J., Charpentier, B., Pilgrim, W.R., Reichert, U., and Shroot, B. (1992). Identification of synthetic retinoids with selectivity for human nuclear retinoic acid receptor-gamma. *Biochemical and Biophysical Research Communications* **186**, 977-983.

Buxboim, A., Rajagopal, K., Brown, A.E.X., and Discher, D.E. (2010). How deeply cells feel: methods for thin gels. *Journal of Physics-Condensed Matter* **22**.

Gambone, C.J., Hutcheson, J.M., Gabriel, J.L., Beard, R.L., Chandraratna, R.A.S., Soprano, K.J., and Soprano, D.R. (2002). Unique property of some synthetic retinoids: Activation of the aryl hydrocarbon receptor pathway. *Molecular Pharmacology* **61**, 334-342.

Majkut, S., Idema, T., Swift, J., Krieger, C., Liu, A., and Discher, D.E. (2013). Heart-Specific Stiffening in Early Embryos Parallels Matrix and Myosin Expression to Optimize Beating. *Current Biology* **23**, 2434-2439.

Neuman, R.E., and Logan, M.A. (1950). The determination of collagen and elastin in tissues. *Journal of Biological Chemistry* **186**, 549-556.

Pajerowski, J.D., Dahl, K.N., Zhong, F.L., Sammak, P.J., and Discher, D.E. (2007). Physical plasticity of the nucleus in stem cell differentiation. *Proceedings of the National Academy of Sciences of the United States of America* **104**, 15619-15624.

Shimozono, S., Imura, T., Kitaguchi, T., Higashijima, S., and Miyawaki, A. (2013). Visualization of an endogenous retinoic acid gradient across embryonic development. *Nature* **496**, 363-366.

Shroot, B., and Michel, S. (1997). Pharmacology and chemistry of adapalene. *Journal of the American Academy of Dermatology* **36**, 96-103.

Swift, J., Harada, T., Buxboim, A., Shin, J.-W., Tang, H.-Y., Speicher, D.W., and Discher, D.E. (2013a). Label-free mass spectrometry exploits dozens of detected peptides to quantify lamins in wildtype and knockdown cells. *Nucleus-Austin* **4**, 450-459.

Swift, J., Ivanovska, I.L., Buxboim, A., Harada, T., Dingal, P.C.D.P., Pinter, J., Pajeroski, J.D., Spinler, K.R., Shin, J.-W., Tewari, M., Rehfeldt, F., Speicher, D.W., and Discher, D.E. (2013b). Nuclear lamin-A scales with tissue stiffness and enhances matrix-directed differentiation. *Science* **341, 1240104.**

Szondy, Z., Reichert, U., Bernardon, J.M., Michel, S., Toth, R., Ancian, P., Ajzner, E., and Fesus, L. (1997). Induction of apoptosis by retinoids and retinoic acid receptor gamma-selective compounds in mouse thymocytes through a novel apoptosis pathway. *Molecular Pharmacology* **51, 972-982.**

Zemel, A., Rehfeldt, F., Brown, A.E.X., Discher, D.E., and Safran, S.A. (2010). Optimal matrix rigidity for stress-fibre polarization in stem cells. *Nature Physics* **6, 468-473.**

Zou, L.J., Luo, Y.L., Chen, M.W., Wang, G., Ding, M., Petersen, C.C., Kang, R., Dagnaes-Hansen, F., Zeng, Y.L., Lv, N.H., Ma, Q., Le, D.Q.S., Besenbacher, F., Bolund, L., Jensen, T.G., Kjems, J., Pu, W.T., and Bunger, C. (2013). A simple method for deriving functional MSCs and applied for osteogenesis in 3D scaffolds. *Scientific Reports* **3.**